RB1 deficiency in triple-negative breast cancer induces mitochondrial protein translation

Robert A. Jones,[1] Tyler J. Robinson,[1] Jeff C. Liu,[1] Mariusz Shrestha,[1,2] Veronique Voisin,[3] YoungJun Ju,[1] Philip E.D. Chung,[1,2] Giovanna Pellecchia,[2] Victoria L. Fell,[1] SooIn Bae,[4] Lakshmi Muthuswamy,[5] Alessandro Datti,[6,7] Sean E. Egan,[8,9] Zhe Jiang,[1] Gustavo Leone,[4] Gary D. Bader,[3,9] Aaron Schimmer,[10] and Eldad Zacksenhaus[1,2,11]

[1]Division of Advanced Diagnostics, Toronto General Research Institute, University Health Network, Toronto, Ontario, Canada. [2]Department of Laboratory Medicine and Pathobiology, University of Toronto, Toronto, Ontario, Canada. [3]The Donnelly Centre, University of Toronto, Toronto, Ontario, Canada. [4]Department of Molecular Genetics, Ohio State University, Columbus, Ohio, USA. [5]Ontario Institute for Cancer Research, Toronto, Ontario, Canada. [6]SMART Laboratory for High-Throughput Screening Programs, Lunenfeld-Tanenbaum Research Institute at Mount Sinai Hospital, Toronto, Ontario, Canada. [7]Department of Agricultural, Food and Environmental Sciences, University of Perugia, Perugia, Italy. [8]Program in Developmental Biology, The Hospital for Sick Children, Toronto, Ontario, Canada. [9]Department of Molecular Genetics, University of Toronto, Toronto, Ontario, Canada. [10]Princess Margaret Cancer Center, Toronto, Ontario, Canada. [11]Department of Medicine, University of Toronto, Toronto, Ontario, Canada.

Triple-negative breast cancer (TNBC) includes basal-like and claudin-low subtypes for which no specific treatment is currently available. Although the retinoblastoma tumor-suppressor gene (*RB1*) is frequently lost together with *TP53* in TNBC, it is not directly targetable. There is thus great interest in identifying vulnerabilities downstream of *RB1* that can be therapeutically exploited. Here, we determined that combined inactivation of murine *Rb* and *p53* in diverse mammary epithelial cells induced claudin-low–like TNBC with *Met*, *Birc2/3-Mmp13-Yap1*, and *Pvt1-Myc* amplifications. Gene set enrichment analysis revealed that *Rb/p53*-deficient tumors showed elevated expression of the mitochondrial protein translation (MPT) gene pathway relative to tumors harboring *p53* deletion alone. Accordingly, bioinformatic, functional, and biochemical analyses showed that RB1-E2F complexes bind to MPT gene promoters to regulate transcription and control MPT. Additionally, a screen of US Food and Drug Administration–approved (FDA-approved) drugs identified the MPT antagonist tigecycline (TIG) as a potent inhibitor of *Rb/p53*-deficient tumor cell proliferation. TIG preferentially suppressed *RB1*-deficient TNBC cell proliferation, targeted both the bulk and cancer stem cell fraction, and strongly attenuated xenograft growth. It also cooperated with sulfasalazine, an FDA-approved inhibitor of cystine xCT antiporter, in culture and xenograft assays. Our results suggest that *RB1* deficiency promotes cancer cell proliferation in part by enhancing mitochondrial function and identify TIG as a clinically approved drug for *RB1*-deficient TNBC.

Introduction

Breast cancer (BC) is a leading cause of cancer-related deaths in women worldwide. It can be classified into at least 5 molecular subtypes: luminal A, luminal B, human EGFR 2–overexpressing (HER2-overexpressing), basal-like, and claudin-low (1–4). Most basal-like and claudin-low tumors are categorized as triple-negative BCs (TNBCs), as they lack expression of hormone receptors (estrogen receptor [ER], progesterone receptor [PR]) and HER2 and consequently resist the targeted therapies available for patients with ERα$^+$ and HER2$^+$ BC. Although TNBCs respond to standard chemotherapy, less toxic treatments with more specificity are urgently needed.

The TP53 and RB1 tumor suppressors are frequently altered in BC, particularly in TNBCs (3, 4). Indeed, we previously showed that deletion of murine *Rb* in mammary epithelium via mouse mammary tumor virus long terminal repeat promoter–driven *Cre* (*MMTV-Cre*)induced luminal B and TNBC-like tumors, with the latter containing dominant-negative p53 mutations, demonstrating a causal effect of *Rb* in BC (5). Furthermore, orthotopic transplantation of primary mammary epithelial cells (MECs) from several independent *MMTV-Cre* $Rb^{fl/fl}$ $p53^{fl/fl}$ mice accelerated the formation of spindle-cell/mesenchymal-like tumors.

pRb functions primarily as a transcriptional cofactor; it binds the transactivation domains of activating E2Fs, E2F1/2/3a and recruits chromatin-modifying factors such as histone deacetylases and methylases to silence gene expression. pRb binds a myriad of other cellular proteins (6, 7), but it exerts its effects on cell proliferation and survival primarily through the regulation of activating E2Fs (8–10). Indeed, major targets of pRb-E2F are genes involved in cell-cycle progression and apoptosis (10–14). While deregulation of cell proliferation due to pRb loss promotes cancer, the sensitization of Rb-deficient cells to apoptosis precludes aberrant growth under nonpermissive conditions such as limited growth signals. Therefore, in most types of cancer, pRb inactivation is accompanied by the induction of prosurvival pathways such as p53 inactivation.

RB1 loss is not directly druggable (15, 16). However, it is conceivable that pathways downstream of this tumor suppressor are actionable. For example, many oncogenic events promote rapid cell proliferation by redirecting glucose and glutamine into anabolic pathways (17–20). In *Drosophila*, the pRb homolog Rbf has

Authorship note: R.A. Jones, T.J. Robinson, J.C. Liu, M. Shrestha, and V. Voisin contributed equally to this work.
Conflict of interest: The authors have declared that no conflict of interest exists.
Submitted: February 18, 2015; **Accepted:** July 12, 2016.
Reference information: *J Clin Invest*. doi:10.1172/JCI81568.

been implicated in regulating nucleotide synthesis and glutathione (GSH) metabolism, though this effect was not consistently seen in RB1-negative mammalian cancer cells (21). Deletion of all 3 members of the Rb gene family (*Rb*, *p107*, and *p130*) in mouse embryonic fibroblasts (MEFs) induces GSH metabolism (22), whereas deletion of *Rb* alone in primary cells alters cell metabolism, mitochondrial function, and mitophagy (23–26). Interestingly, following the initial submission of this manuscript, it was reported that *RB1* loss suppresses oxidative phosphorylation (OXPHOS) in noncancerous cells (27). The effect of *RB1* loss on metabolism in cancer cells and whether this effect is amenable to therapeutic intervention are largely unknown.

To address this issue, we generated and compared histologically similar Rb/p53- and p53-deficient mammary tumors for vulnerabilities that can be exploited for therapy. We have found that, relative to p53-deficient tumors, combined loss of *Rb* and *p53* induced tumors with elevated mitochondrial protein translation (MPT) pathway and sensitivity to tigecycline (TIG), an MPT inhibitor. TIG monotherapy efficiently suppressed growth of human RB1/TP53-deficient TNBC cells in culture as well as in xenograft assays. Collectively, our results indicate that *RB1* loss reprograms cancer metabolism not toward anabolic pathways but toward enhanced mitochondrial function. This effect is mediated through direct transcriptional activation of MPT genes by activating E2Fs, suggests that combined loss of *RB1* and *TP53* may cooperate in cancer cells to promote aggressive cancer metabolism, and points to TIG as a potential new therapeutic for RB1-deficient TNBC.

Results

Frequent loss of both RB1 and TP53 in basal-like BC. Genomic and proteomic analyses indicate that RB1 is lost in approximately 20% to 30% of basal-like BCs, while TP53 is disrupted in 50% to 80% of basal-like BCs (3, 4). To estimate the frequency of tumors with alterations in both *RB1* and *TP53*, we manually identified these tumors using cBioPortal (http://cbioportal.org) and The Cancer Genome Atlas (TCGA) data sets (Figure 1A). Concurrent *RB1* and *TP53* alterations were found in nearly 40% of basal-like BC, which was a significantly higher percentage than that detected in other subtypes (P = 0.00151; Figure 1B). The overlap coefficient for combined *RB1* and *TP53* alterations in basal-like BC was high (0.94) but not significant due to very high *TP53* mutation rates in this subtype (88%). When all BC subtypes were compared, the overlap coefficient was high and significant (0.78, $P = 4.34 \times 10^{-9}$), indicating preferential concomitant loss of *RB1* and *TP53* in BC.

We also estimated the frequency of combined loss of these tumor suppressors using a *TP53* pathway activity signature (Sig) developed by Gatza et al. (28, 29) and an *RB1* loss Sig from Herschkowitz et al. (30). The advantage of using these Sigs is that they capture divergent mechanisms of loss of function of these tumor suppressors. We used PAM50 to molecularly classify 1,500 patients (Supplemental Figure 1; supplemental material available online with this article; doi:10.1172/JCI81568DS1)(29). Notably, PAM50 does not differentiate between different TNBC subgroups, and the basal tumors include basal-like, claudin-low, and other lesions.

Of the 20 *RB1* loss Sig genes, 18 were reproducibly found in our microarray datasets. When examined individually, tumors with both an *RB1* loss Sig (RB Sig$^+$) and TP53 pathway activity-low (p53^{lo}) were predominantly basal (Figure 1C; 131 of 636 = 36% and 240 of 363 = 66%, respectively). As with TCGA analysis above, *RB1-TP53* double loss was found predominantly in basal-like tumors (27.8%), followed by HER2$^+$ and luminal B tumors, with none found in luminal A or normal-like tumors (P = 0.000372; Figure 1D). Importantly, co-occurrence of RB Sig$^+$ and p53^{lo} was highly significant, with an overlap coefficient of 0.77 ($P = 5.69 \times 10^{-4}$) in basal-like tumors and 0.56 ($P = 2.53 \times 10^{-32}$) in all subtypes (Figure 1E). Thus, 2 different approaches show that combined *RB1-TP53* loss occurs frequently (28%–40%) in basal-like/TNBC.

Disruption of murine Rb and p53 in divergent MECs, including luminal progenitors, induces mammary tumors with features of EMT. To model combined *RB1-TP53* loss in BC, we disrupted both tumor suppressors using different deleter lines or sorted cell populations. Specifically, we transplanted primary MECs from *MMTV-Cre* $Rb^{fl/fl}$ $p53^{fl/fl}$ females or from mid-pregnancy (15 dpc) *Wap-Cre* $Rb^{fl/fl}$ $p53^{fl/fl}$ females (using the whey acidic protein [*Wap*] *Cre*, which targets alveolar progenitors) (31), into mammary glands of the recipient mice (Figure 2A and Supplemental Figure 2), or isolated MECs from $Rb^{fl/fl}$ $p53^{fl/fl}$ mice (i.e., *Cre* negative) and then used adenoviral-*Cre* (Ad-*Cre*) to delete *Rb* and *p53* ex vivo prior to transplantation (Figure 2A, Supplemental Figure 2, and Supplemental Figure 3). We also monitored cohorts of nulliparous *MMTV-*Cre^{NLST} $Rb^{fl/fl}$ $p53^{fl/fl}$ and *MMTV-Cre* $Rb^{fl/fl}$ $p53^{LSLR270H/+}$ animals, in which *Rb* is deleted together with *p53*, or in which a p53-R270H point mutation is expressed (5, 32, 33). Many of these transgenic mice succumbed to lymphomas, but surviving animals developed mammary tumors, albeit with longer latency. In all cases, mammary tumors shared similar spindle-shape histology, expressed high levels of the mesenchymal markers vimentin, desmin, and N-cadherin, but not the luminal marker E-cadherin, and were histologically classified as adeno-sarcomatoid/spindle-cell/mesenchymal–like BC (Figure 2, B and C, and Supplemental Figure 2, H–J). Spindle-cell tumors have been observed in a number of other mouse BC models and were shown to be similar to human claudin-low BC (34). These tumors exhibit low expression of tight-junction proteins, including claudins 3, 4, and 7 and E-cadherin, as well as high expression of genes associated with epithelial-to-mesenchymal transition (EMT), stem cell–like properties, and immune response (1, 35), share a gene Sig derived from tumor-initiating cells (TICs)/cancer stem cells (CSCs), and are clinically associated with poor outcome (36, 37).

The aforementioned results suggest that combined inactivation of *Rb* plus *p53* can induce claudin-low–like tumors from divergent epithelial cell populations, not only from mammary stem cells, as is widely thought (38–41). However, while the *Cre* drivers used above target different cells along the mammary epithelial hierarchy, their expression patterns do overlap to some extent. Therefore, to test the effect of *Rb* plus *p53* mutation specifically in luminal versus basal progenitors, we disrupted these genes in enriched populations of luminal or basal progenitors. Primary MECs were isolated from $Rb^{fl/fl}$ $p53^{fl/fl}$ mice, FACS sorted into luminal and basal cell subpopulations using CD24, a luminal marker, and CD49f (α6 integrin), a basal marker (42, 43), and seeded into 3D Matrigel culture (Supplemental Figure 3A). Under these conditions, CD24^{hi}CD49f^{lo} luminal progenitors formed large structures with a hollow acini-like appearance, whereas CD24^{lo}CD49f^{hi} basal

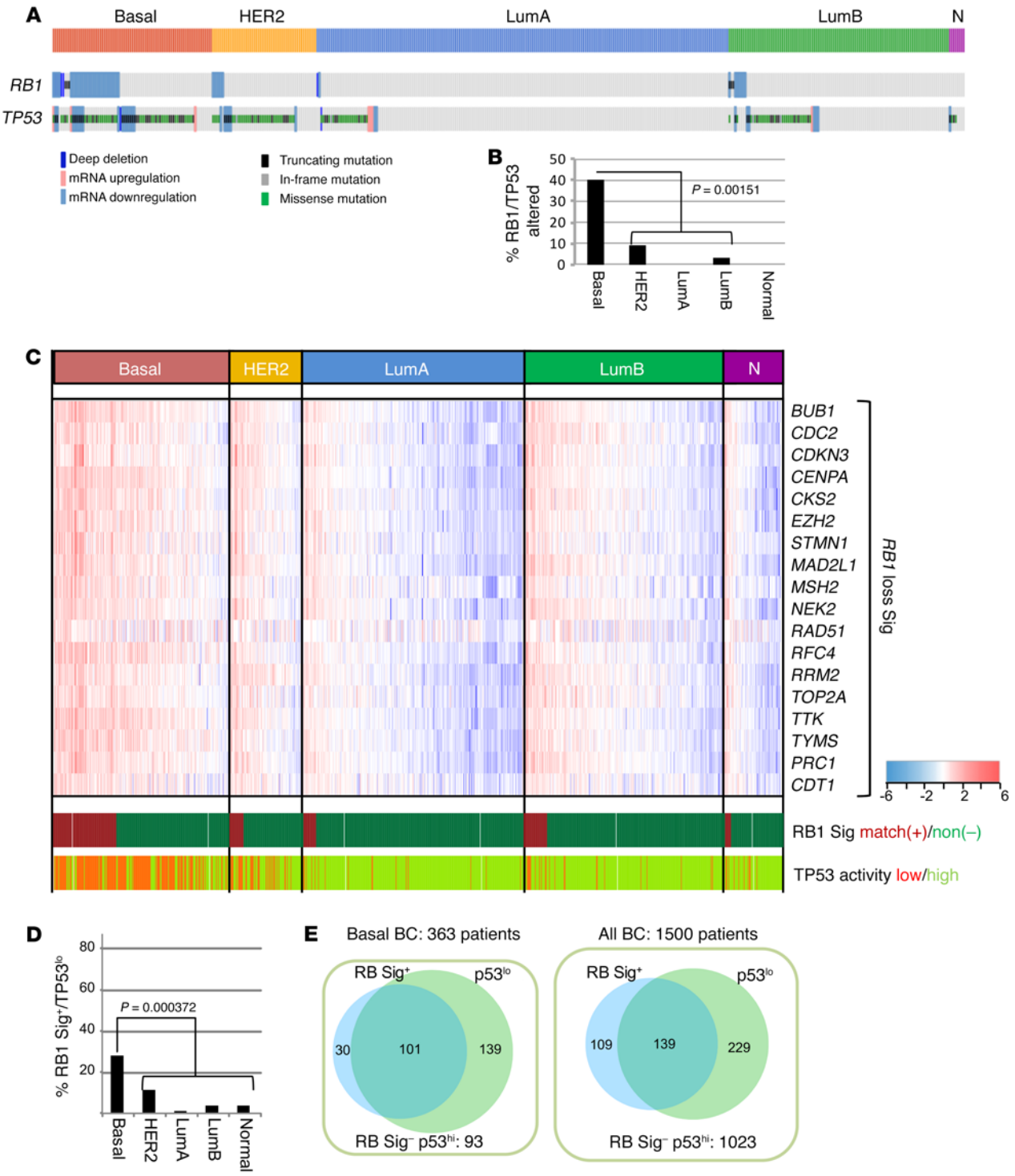

Figure 1. RB1 and TP53 are frequently lost together in TNBC. (**A**) Oncoprint plot of RB1 and TP53 alterations in the Breast Invasive Carcinoma, TCGA data set (n = 463 complete samples with mutation, copy number, and expression data). The overlap coefficient of combined RB1 and TP53 loss was 0.94 (P = 0.121) in basal BC and 0.78 ($P = 4.34 \times 10^{-9}$) in all BC subtypes. (**B**) Percentage of tumors from major molecular subtypes with alterations in both RB1 and TP53. Patients with basal BC showed frequent alterations in both RB1 and TP53 relative to other subtypes (40%; P = 0.00151, by Kruskal-Wallis test). (**C**) Patients with *RB1* loss of function identified using an 18-gene *RB1* loss Sig. (**D**) A significantly higher percentage of basal tumors was RB Sig$^+$ p53^{lo} (~28%, P = 0.000372, by Kruskal-Wallis test) compared with all other subtypes. (**E**) Venn diagrams showing overlaps between RB Sig$^+$ and TP53^{lo} in basal BC and all BC samples. Significant overlaps between RB Sig$^+$ and TP53^{lo} were observed in both groups: basal BC = 0.77 ($P = 5.69 \times 10^{-4}$); all BC = 0.56 ($P = 2.53 \times 10^{-32}$). LumA, luminal A; LumB, luminal B; N, normal-like.

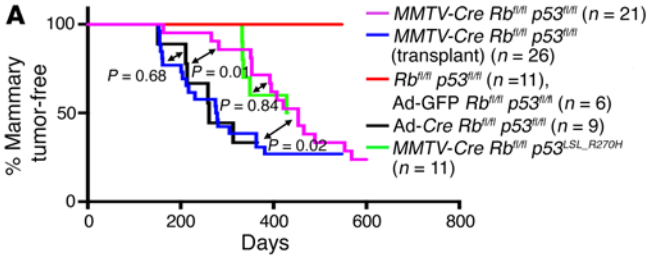

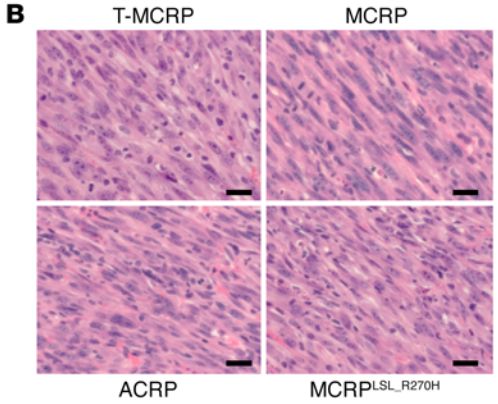

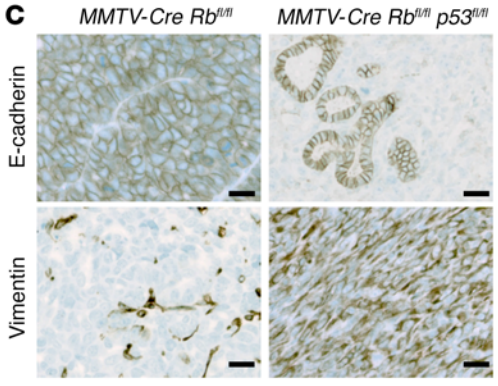

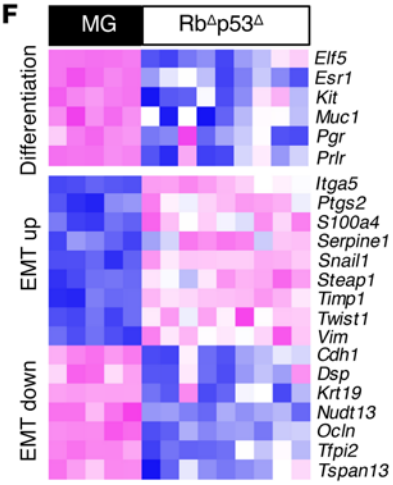

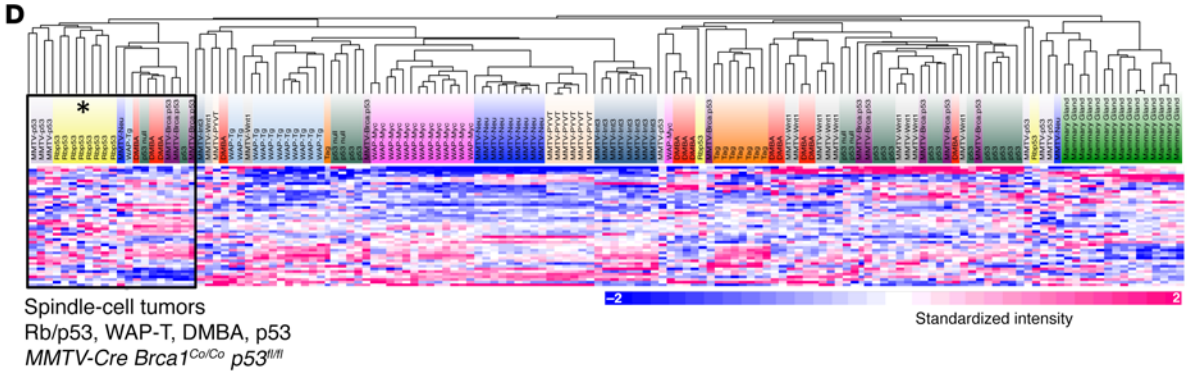

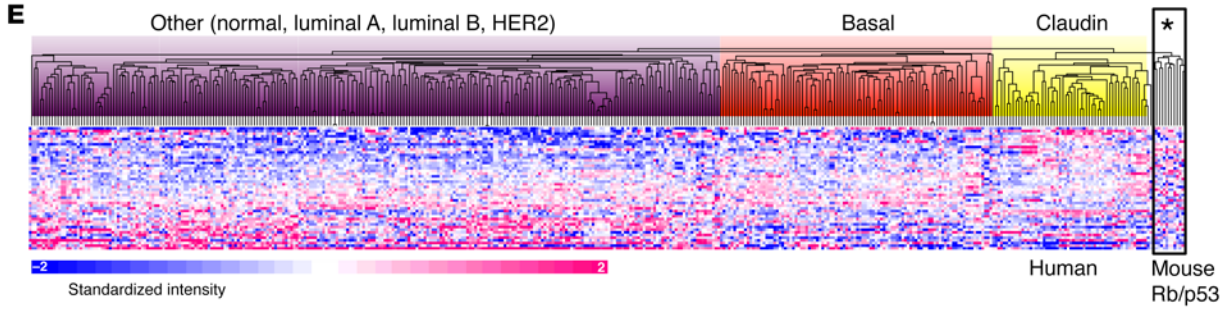

Figure 2. Disruption of Rb and p53 through diverse *Cre* drivers induces spindle-cell tumors that cluster with human claudin-low BC. (**A**) Kaplan-Meier mammary tumor-free survival curves of the indicated mouse or transplantation models used to disrupt Rb and p53. *P* values were determined by log-rank test. (**B**) Histology of mammary tumors from *MMTV-Cre Rb$^{fl/fl}$ p53$^{fl/fl}$* transplanted cells (T-MCRP), *MMTV-Cre Rb$^{fl/fl}$* mice (MCRP), Ad-*Cre Rb$^{fl/fl}$ p53$^{fl/fl}$* transplanted cells (ACRP), or *MMTV-Cre Rb$^{fl/fl}$ p53$^{LSLR270H/+}$* mice showing very similar spindle-cell morphology with numerous mitotic cells. (**C**) Immunostaining for vimentin (mesenchymal marker) and E-cadherin (luminal marker) of an adenocarcinoma (left) and spindle-cell carcinoma (right) isolated from the indicated mice. Note the widespread expression of E-cadherin in Rb-deficient adenocarcinoma, but only in normal epithelial ducts in Rb/p53-deficient spindle tumors. (**D**) Cluster analysis comparing Rb$^{\Delta}$p53$^{\Delta}$ tumors (indicated by an asterisk) with 13 different BC mouse models showing resemblance to other models of spindle-like tumors. *MMTV-Cre Brca$^{Co/Co}$ p53$^{+/-}$*, *Brca* floxed, *p53* heterozygous. (**E**) Cluster analysis of Rb$^{\Delta}$p53$^{\Delta}$ tumors with human BC using a human claudin-low predictor. Blue (low expression); magenta (high expression). Asterisk indicates the location of the Rb/p53 mouse samples. (**F**) Heatmap of EMT and claudin-low–related markers in Rb/p53-deficient spindle-cell mammary tumors relative to normal mammary glands. Scale bars: 50 μm (**B** and **C**). up, upregulation; down, downregulation.

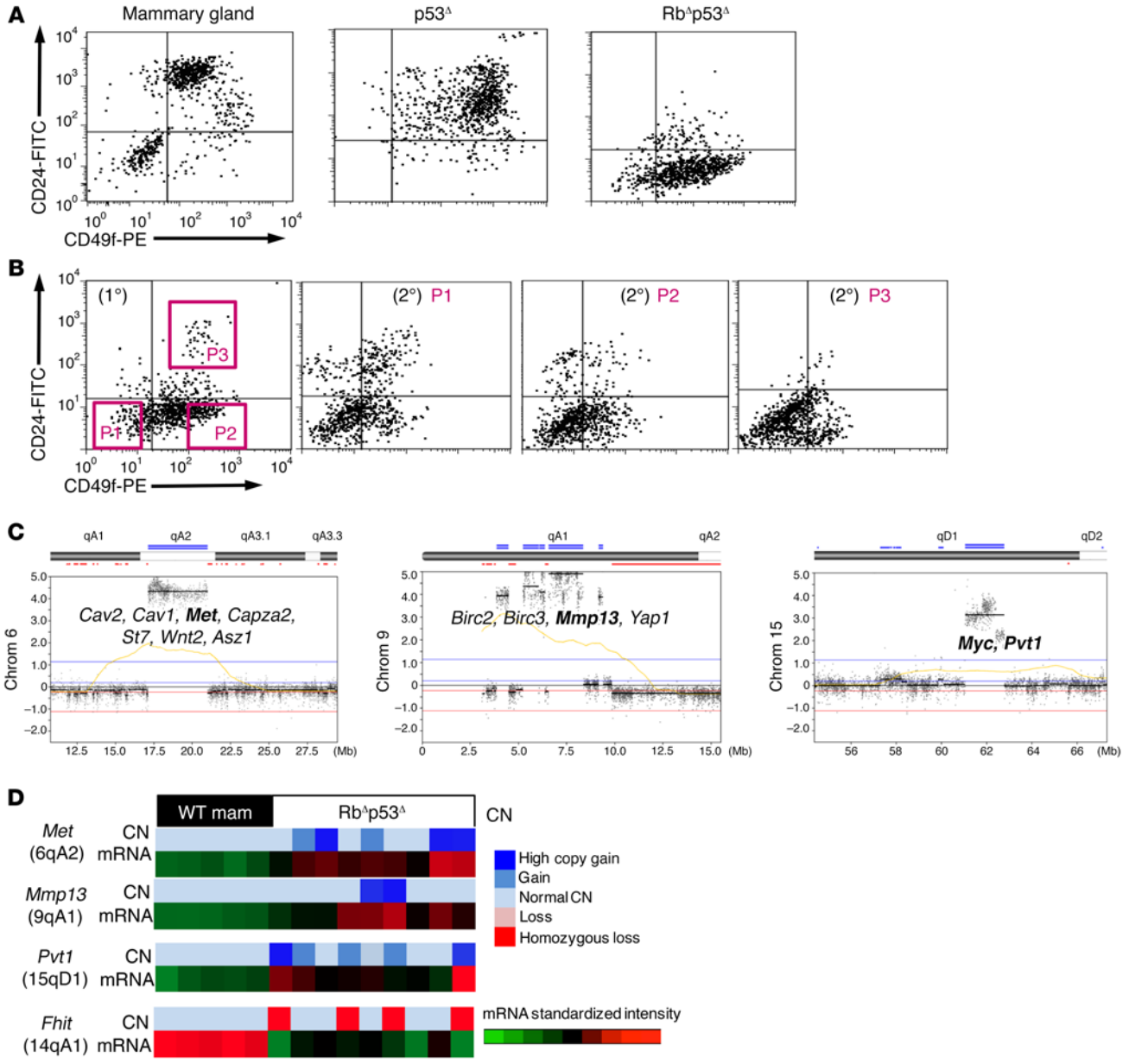

Figure 3. Rb/p53-deficient mammary tumors show a high frequency of CD49f$^+$CD24$^-$ TICs and genomic amplifications involving *Met*, *Birc2/3-Mmp13-Yap1*, and *Pvt1-Myc*. (**A**) Flow cytometric profiles of normal mammary gland and p53$^\Delta$ and Rb$^\Delta$p53$^\Delta$ claudin-low mammary tumors with CD49f and CD24 cell-surface markers. (**B**) Gates used to isolate tumor cell populations (1°). FACS profiles of secondary tumors obtained from CD49f^{lo}CD24^{lo} (P1), CD49f^{hi}CD24^{lo} (P2), and CD49f^{hi}CD24^{hi} (P3) populations (2°). See Table 1 for TIC frequency. (**C**) Probe level images of copy number data showing high-level amplifications on chromosomes (Chrom) 6qA2, 9qA1, and 15qD1. (**D**) Integration of CNAs with gene expression identified genes regulated at the genomic and transcriptional levels, including *Met*, *Pvt1*, and *Mmp13* amplification as well as *Fhit* deletion on chromosome 14qA1. Green (low); red (high). CN, copy number; mam, mammary; PE, phycoerythrin.

cell populations formed solid spheres (Supplemental Figure 3E, top) (44). Luminal and basal cells rarely gave rise to organoids of the other type (<0.05%). Following dissociation of the *Rb$^{fl/fl}$ p53$^{fl/fl}$* organoids into single cells, luminal or basal cells were transduced with Ad-*Cre*, which targets both mammary stem cells (MaSCs) and non-MaSCs (45), and immediately transplanted into cleared fat pads of immune-deficient mice. To provide a similar cellular milieu, infected luminal and basal cells were mixed (1:1 ratio) in some experiments with lineage-depleted (CD45$^-$CD31$^-$Tert119$^-$) cells, supporting MECs before transplantation. Following orthotopic injection, a higher frequency of tumors was developed from luminal progenitors relative to basal progenitors (76% vs. 46%), though this did not reach statistical significance ($P = 0.1322$, Fisher's exact test; Supplemental Figure 3, F and G). However, tumor onset for the luminal progenitor population was shorter compared with that of the basal population (median onset of 74 vs. 148 days, $P = 0.0093$, log-rank test). Importantly, all tumors from both luminal- and basal-derived cell populations exhibited a spindle cell

Table 1. Enrichment of Rb$^{\Delta}$p53$^{\Delta}$ TICs in Lin^{-}CD49f^{hi}CD24^{lo} and Lin^{-}CD49f^{lo}CD24^{lo} cell subpopulations

Cells injected	1,000	250	100	50	10	TIC frequency (95% CI)
P1 (Lin^{-}CD49f^{lo}CD24^{lo})	6/8	4/4	5/10	2/4	4/10	1/220 (1/115–1/422)[A]
P2 (Lin^{-}CD49f^{hi}CD24^{lo})	7/8	2/4	6/10	1/4	4/8	1/197 (1/103–1/379)[B]
P3 (Lin^{-}CD24^{hi}CD49f^{hi})	6/8	1/4	2/10	1/4	0/8	1/635 (1/318–1/1,230)

[A]P1 versus P3, $P = 0.0295$; [B]P2 versus P3, $P = 0.0163$.

histology that was indistinguishable from that seen in *MMTV-Cre Rb$^{fl/fl}$ p53$^{fl/fl}$* and *Wap-Cre Rb$^{fl/fl}$ p53$^{fl/fl}$* mice or in Ad-*Cre*–infected bulk mammary cells (Supplemental Figure 3E). Together, these results suggest that, in the context of combined Rb plus p53 deficiency, spindle-cell tumors can arise from luminal progenitors and possibly from both the luminal and basal compartments.

Rb/p53-deficient mammary tumors cluster with human claudin-low BC and exhibit highly mesenchymal TICs and alterations in the Met, Birc2/3-Mmp13-Yap1, Pvt1-Myc, and Fhit loci. To molecularly classify the Rb/p53-deficient mammary tumors, we performed inter- and cross-species comparison of gene expression profiles (35). Most Rb$^{\Delta}$p53$^{\Delta}$ mouse mammary tumors (9 of 10) clustered closely with other mouse spindle-cell tumors (7,12-dimethylbenz[a]anthracene–treated [DMBA-treated] *MMTV-Cre Brca1$^{Co/Co}$ p53$^{+/-}$* and *MMTV-Cre p53$^{fl/fl}$* mouse tumors; Figure 2D). Furthermore, using a claudin-low predictor developed by Prat and Perou (46), 9 of 10 of the Rb$^{\Delta}$p53$^{\Delta}$ tumors clustered most closely, albeit as a distinct group as expected from cross-species comparison, with human claudin-low TNBC (Figure 2E). Consistent with a claudin-low–like classification, the mouse Rb/p53-deficient spindle-cell tumors expressed low levels of differentiation markers (*Elf5*, *Muc1*, *Prlr*) and claudins and cell adhesion markers (*Cdh1*, *Ocln*), as well as high levels of EMT inducers such as *Snail1* and *Twist1* (Figure 2F).

Mouse mammary tumors, including p53-deficient, MMTV-Neu, and MMTV-WNT1 tumors, exhibit prominent CD49f^{hi}CD24^{hi} cell populations enriched in TICs (43, 47). In contrast, the Rb$^{\Delta}$p53$^{\Delta}$ claudin-low tumors expressed very low levels of CD24 and were mostly CD49f^{hi}CD24^{lo} or CD49f^{lo}CD24^{lo} double negative (Figure 3A). Serial dilutions and transplantation assays revealed that TICs were present at a significantly higher frequency within the CD49f^{lo}CD24^{lo} and CD49f^{hi}CD24^{lo} fractions (1 of 220 and 1 of 197, respectively), compared with the CD49f^{hi}CD24^{hi} compartment (1 of 635; $P < 0.03$; Table 1). Secondary tumors exhibited flow cytometric profiles similar to those of the primary tumors from which they were derived (Figure 3B). Thus, most Rb$^{\Delta}$p53$^{\Delta}$ TICs did not express the CD24 luminal marker, underscoring their highly mesenchymal characteristics.

To identify oncogenic networks that cooperate with *Rb/p53* loss to induce claudin-low–like TNBC, we performed array comparative genomic hybridization (aCGH) analysis. Numerous DNA copy number aberrations, including low-level copy number alterations (CNAs), were identified and involved gains of large portions of chromosomes 3, 5, 8, and 15, as well as losses affecting chromosomes 1, 2, 7, and 12 (Supplemental Figure 4, A and B). Further examination of high-level gains and homozygous losses (using $\log_2$ ratio thresholds of 1.14 and –1.1, respectively) identified focal amplifications at the 6qA2 locus (in 5 of 9 tumors), which includes the caveolins (*Cav1*, *Cav2*), *Met*, *ST7*, *Wnt2*, *Asz1*, and a *Cftr* cluster; 9qA1 (orthologous to human 11q22, in 2 of 9 tumors), which encompasses the proto-oncogenes *Yap1* and *cIAP1* (also known as *Birc2*), *cIAP2* (also known as *Birc3*), and a cluster of MMP genes; 15qD1 (syntenic with human 8q24, in 5 of 9 samples), which contains the *Pvt1* and *c-Myc* oncogenes; as well as a homozygous deletion at 14qA1 (orthologous to the fragile site at human 3p14.2, in 4 samples), which harbors the putative tumor suppressor *Fhit* (48, 49) (Figure 3C and Supplemental Figure 4, C and D). Notably, the *Birc-MMP-Yap1* and *Met* amplicons were previously identified in Rb/p53- and p53-deficient mouse tumors (50, 51).

Integration of the copy number data with matched gene expression profiles revealed that *Met*, *Mmp13*, and *Pvt1* were highly expressed at the mRNA level in tumors with amplified 6qA2, 9qA1, and 15qD1, respectively, and that *Fhit* mRNA was downregulated in tumor samples that showed copy number loss (Figure 3D). In accordance, the MET inhibitor crizotinib (52) and the MMP13-specific inhibitor WAY-170523 (53) suppressed growth of our Rb$^{\Delta}$p53$^{\Delta}$ tumor cells in a dose-dependent manner (Supplemental Figure 5). Collectively, these results indicate that Rb/p53 deficiency induces highly mesenchymal tumors that resemble human claudin-low TNBC, contain CD24^{-} TICs, and show a high incidence of chromosomal gains and losses, including specific alterations in *Met*, *Birc2/3-Mmp13-Yap1*, *Pvt1-Myc*, and *Fhit*.

Bioinformatic analysis identifies an elevated MPT pathway in Rb/p53-deficient versus p53-deficient tumors. To identify potentially novel therapeutic targets for Rb-deficient TNBC, we performed gene set enrichment analysis (GSEA) (54), combined with Enrichment Map (55, 56) (Figure 4A). Overall, there were fewer significantly (FDR ≤ 0.05) enriched gene sets in claudin-low p53$^{\Delta}$ tumors relative to claudin-low Rb$^{\Delta}$p53$^{\Delta}$ tumors, which primarily involved immune response. Upregulated in Rb$^{\Delta}$p53$^{\Delta}$ relative to p53$^{\Delta}$ tumors were pathways indicative of a stem cell/primitive differentiation state including EMT, fetal development, and WNT signaling. Consistent with the known effects of *Rb* loss, mitosis and cell cycle, apoptosis, and DNA damage and repair pathways were also enriched in upregulated genes. Importantly, several pathways associated with cellular metabolism were induced in Rb$^{\Delta}$p53$^{\Delta}$ versus p53$^{\Delta}$ tumors, including MPT, the TCA cycle, nucleotide metabolism, and GSH transferase.

Activation of metabolic pathways in Rb$^{\Delta}$p53$^{\Delta}$ versus p53$^{\Delta}$ tumors could be indirect, through an oncogenic event that cooperates with *Rb* loss, or direct, through transcriptional deregulation by its partners such as activating E2F1-3. To address the latter possibility, we first asked whether promoters of MPT genes upregulated in Rb$^{\Delta}$p53$^{\Delta}$ tumors contain consensus E2F–binding sites. We identified 89 upregulated MPT genes in "mitochondrial organization" (Gene Ontology [GO] ID: 0007005); "mitochondrial part" (GO ID: 0044429); "mitochondrial matrix" (GO ID: 0005729); "organellar ribosome" (GO ID: 0000313); and "mitochondrial ribosome" (GO ID: 0005761) gene sets (Figure 4, B and C). We then searched for

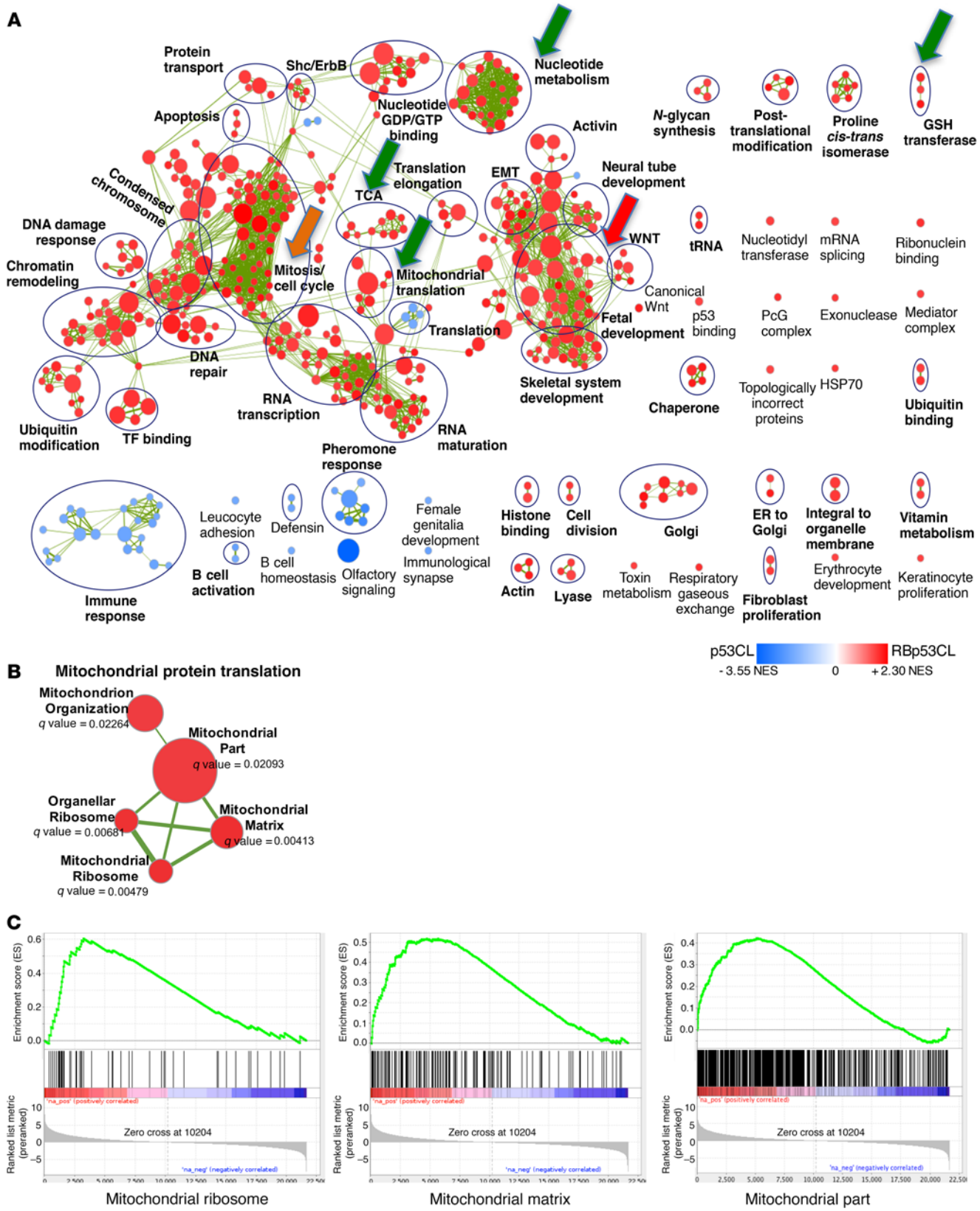

Figure 4. Pathway analysis of Rb/p53- versus p53-deficient tumors reveals induction of the MPT pathway. (**A**) GSEA of $Rb^{\Delta}p53^{\Delta}$ (red) versus $p53^{\Delta}$ (blue) claudin-low (CL) mammary tumors. Orange and red arrows point to cell-cycle and EMT/fetal development/WNT pathways, respectively; green arrows point to metabolic pathways including MPT elevated in Rb/p53 tumors. NES, normalized enrichment score; TF, transcription factor. (**B**) Specific MPT pathways induced in Rb/p53- versus p53-deficient tumors. (**C**) Enrichment plots for the indicated MPT pathways.

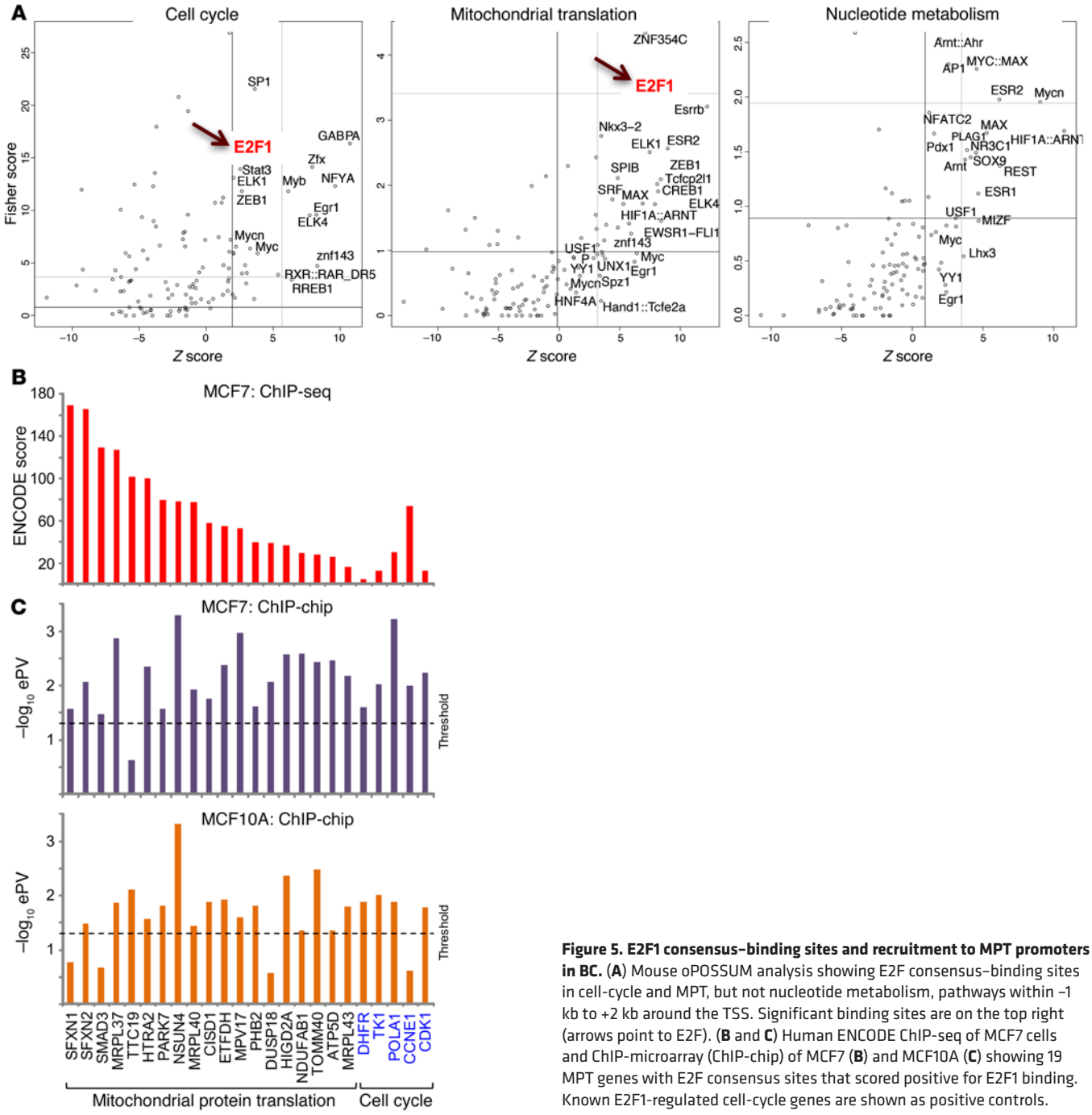

Figure 5. E2F1 consensus–binding sites and recruitment to MPT promoters in BC. (**A**) Mouse oPOSSUM analysis showing E2F consensus–binding sites in cell-cycle and MPT, but not nucleotide metabolism, pathways within –1 kb to +2 kb around the TSS. Significant binding sites are on the top right (arrows point to E2F). (**B** and **C**) Human ENCODE ChIP-seq of MCF7 cells and ChIP-microarray (ChIP-chip) of MCF7 (**B**) and MCF10A (**C**) showing 19 MPT genes with E2F consensus sites that scored positive for E2F1 binding. Known E2F1-regulated cell-cycle genes are shown as positive controls.

overrepresented, conserved transcription factor–binding sequences within +1 kb to –2 kb from the transcription start sites (TSSs) using oPOSSUM 3.0 (57) and found 41 E2F motifs in the vicinity of 26 genes (Supplemental Figure 6A). Compared with 115 other transcription factor motifs (JASPAR database), E2F1 had the third highest Fisher score and the twelfth highest *Z* score, both measures indicating the level of overrepresentation of this motif in the input MPT promoter compared with all genes in the genome (Figure 5A). E2F also ranked high on promoters for "cell cycle" and "E2F-mediated regulation of DNA replication," but poorly on "nucleotide metabolism," "TCA," or "GST transferase" (glutathione S-transferase) pathways (Figure 5A and Supplemental Figure 6B).

To determine whether E2F is actually recruited to promoters of these MPT genes in BC cells, we analyzed ChIP-sequencing (ChIP-seq) data from ENCODE (ENCyclopedia Of DNA Elements) for HA-E2F1 binding in the BC cell line MCF7 (58). Remarkably, of the 26 genes identified by oPOSSUM analysis, 19 were present in the ENCODE data set, indicating direct recruitment of E2F1 to promoter regions surrounding these MPT genes in BC cells (Figure 5B and Supplemental Table 1). Importantly, the ChIP-seq scores were at least as high for MPT genes as for bona fide E2F1–regulated cell-cycle promoters such as dihydrofolate reductase (*Dhfr*) and thymidine kinase (*Tk*; nucleotide synthesis), DNA polymerase α (DNA replication), and cyclin E and *Cdc2*

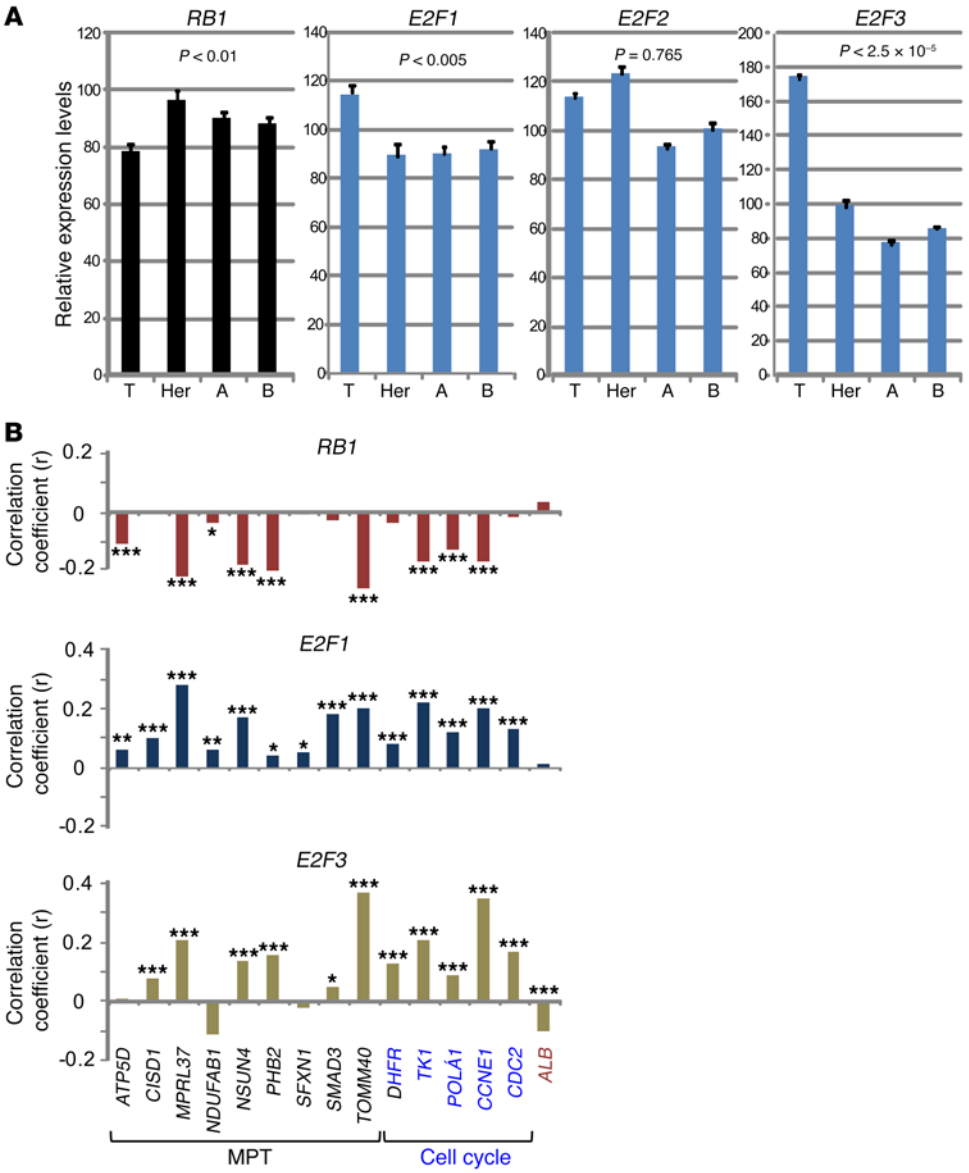

Figure 6. Expression of RB1 and activating E2Fs in BC subtypes in correlation with MPT and cell-cycle genes. (**A**) Relative expression levels of *RB1*, *E2F1*, *E2F2*, and *E2F3* in 1,500 samples of TNBC (T), HER2 (Her), luminal A (A), and luminal B (B) BCs. (**B**) Correlation analysis of *RB1*, *E2F1*, and *E2F3* expression levels with those of the indicated MPT versus known E2F-regulated cell-cycle or albumin genes in 2,228 mixed BC subtypes. $^{*}P < 0.05$, $^{**}P < 0.005$, and $^{***}P < 0.0005$, for the correlation (Pearson's *r*) by a 2-tailed *t* test with n-2 degrees of freedom.

(cell-cycle progression)(59). In addition to localizing at the vicinity of TSSs, the CHIP-seq signals for genes such as *Mrpl37*, *Nsun4*, *Phb2*, *Tomm40*, and *Atp5d* were well aligned with transcriptionally active regions and histone H3K27 acetylation peaks, which mark actively transcribed genes (Supplemental Figure 6, C and D).

Additional evidence for E2F1 recruitment to MPT promoters was obtained using ChIP-chip data from MCF7 BC cells and from the immortalized, basal-like MEC MCF10A (Figure 5C and Supplemental Table 1). To examine whether these MPT genes are affected by deregulated E2F in nontumor cells, we analyzed ChIP-seq data from Rb-null MEFs overexpressing E2F1, E2F3a, or E2F3b (SB and GL, unpublished observations). In these data sets, no E2F1, E2F3a, or E2F3b binding was observed on the 19 MPT genes using the same stringent conditions of +1 kb to –2 kb around the TSS, or a more relaxed window of ± 20 kb (not shown). Thus, efficient recruitment of activating E2Fs to MPT promoters is context specific, as observed in transformed and BC cells but not MEFs.

We next examined levels of the 19 MPT transcripts as a function of *RB1* or *E2F1–3* gene expression in human BC. We first determined expression of *RB1* and *E2F1–3* in 1,500 primary tumors collected from several cohorts with a known subtype. *RB1* transcripts were significantly reduced, whereas *E2F1* and *E2F3*, but not *E2F2*, were significantly elevated in TNBC relative to luminal A, luminal B, or HER^{+} tumors (Figure 6A). To increase the power of our analysis, we analyzed a total of 2,228 BC samples of mixed subtypes for correlation between *RB1/E2F1–3* and MPT mRNA levels. Of the 19 MPT genes from the E2F1 ENCODE^{+} list, 9 (*ATP5D*, *CISD1*, *MRPL37*, *NDUFAB1*, *NSUN4*, *PHB2*, *SFXN1*, *SMAD3*, and *TOMM40*) had a significantly positive correlation with *E2F1* expression, and 6 genes also had a significantly negative correlation with *RB1* and a positive correlation with *E2F3*, but not with *E2F2* (Figure 6B and Supplemental Table 2). Although correlations were modest, ranging from 0.06 to 0.37, they were highly significant; for example, for *MRPL37*, correlations with Rb^{lo}, E2F1-high, or E2F3-high had *P* values of 7.4×10^{-11}, 2.3×10^{-17}, and 5.7×10^{-10}, respectively. Moreover, similar levels of correlation seen with MPT genes were observed with the known E2F-regulated cell-cycle genes (*DHFR*, *TK*, *POLA1*, cyclin *E1*, and *CDC2*), rang-

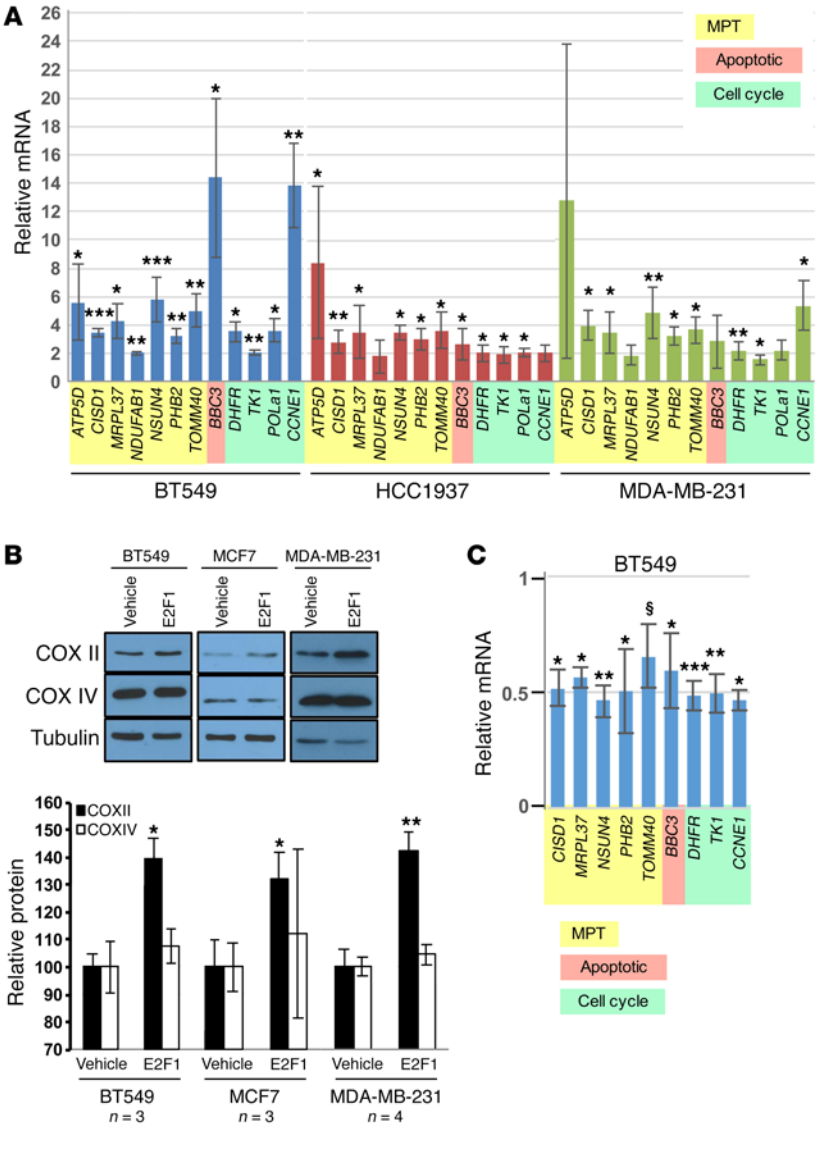

Figure 7. E2F1 and RB1 control MPT gene expression in BC cells. (**A**) Relative fold change in gene expression of MPT, apoptotic, and cell-cycle genes 3 days after Ad-E2F1 and Ad-BCL2 infection compared with control Ad-GFP and Ad-BCL2 in the indicated TNBC cell lines. Values were normalized to *GAPDH* and calibrated to the GFP control ($n = 3$). $^{*}P < 0.05$, $^{**}P < 0.005$, and $^{***}P < 0.0005$, by 2-tailed t test. (**B**) Western blot and quantification of mitochondrially (COX II) and cytosolically (COX IV) translated proteins normalized to tubulin in luminal (MCF7) and TNBC cell lines (BT549 and MDA-MB-231) 3 days after Ad-E2F1 transduction compared with Ad-GFP (vehicle). $^{*}P < 0.05$ and $^{**}P < 0.01$, by 2-tailed t test. (**C**) Relative fold change in gene expression of MPT, apoptotic, and cell-cycle genes 2 days after Ad-RB1 transduction compared with control Ad-GFP in RB1-deficient TNBC cells (BT549). $n = 3$, each performed in triplicate. $^{\S}P = 0.0652$, $^{*}P < 0.05$, $^{**}P < 0.005$, and $^{***}P < 0.0005$, by 2-tailed t test.

ing from 0.08 to 0.35, but not for the negative control albumin (*ALB*) (Figure 6B), suggesting that pRb/E2F1-E2F3 complexes regulate cell-cycle and MPT genes to a similar extent and that both gene sets are independently regulated by additional mechanisms as well. Previous reports documented E2F1-binding sites and/or regulation of the *MRPL37*, *TOMM40*, and *NDUFAB1* promoters (60, 61). Our results demonstrate that these and the other MPT genes are coordinately induced in RB1-deficient BC cells through E2F-binding sites in their promoters.

E2F1 and pRb directly affect MPT expression in TNBC cells. To determine the effect of overexpressing activating E2Fs on MPT gene expression, we initially transduced E2F3a or E2F3b via retroviral vectors into MDA-MB-231, an RB1^{+} TNBC cell line. Stable lines transduced by MYC-E2F3b, which has modest transcription-activating function, expressed high levels of this protein, whereas lines transduced by MYC-E2F3a expressed negligible amounts, suggesting that these cells cannot tolerate overexpression of this factor (Supplemental Figure 7A). Quantitative real-time PCR (qRT-PCR) analysis of the E2F3b-transduced cells versus control GFP–transduced cells revealed a modest increase in the expression of several MPT genes as well as of the bona fide E2F-regulated cell-cycle genes (Supplemental Figure 7B).

Transient transduction of E2F1 via an adenoviral vector at high multiplicities of infection (MOI) led to massive apoptosis 3–4 days after infection (data not shown). To overcome this, we used an approach we used previously to rescue the differentiation defects of Rb-deficient myoblasts by cotransducing the survival factor BCL2 (23). Indeed, coinfection of Ad-E2F1 with Ad-BCL2 markedly reduced apoptosis (data not shown). qRT-PCR under these conditions revealed robust induction of multiple MPT genes in the RB1^{+} line (MDA-MB-231) as well as in the RB1^{-} TNBC lines BT549 and HCC1937 (Figure 7A). Importantly, E2F1 stimulated MPT gene expression to the same extent that it induced known E2F1-regulated cell-cycle genes and the proapoptotic gene *BBC3* (also known as *PUMA*).

The mitochondrial genome encodes 13 mRNAs for OXPHOS subunits that are translated within this organelle. Among these are cytochrome c oxidase I (COX I; *MT-CO1*) and COX II (*MT-CO2*). To ask whether induction of MPT genes by E2F1 would increase mitochondrial translation, we quantified the level of COX II and

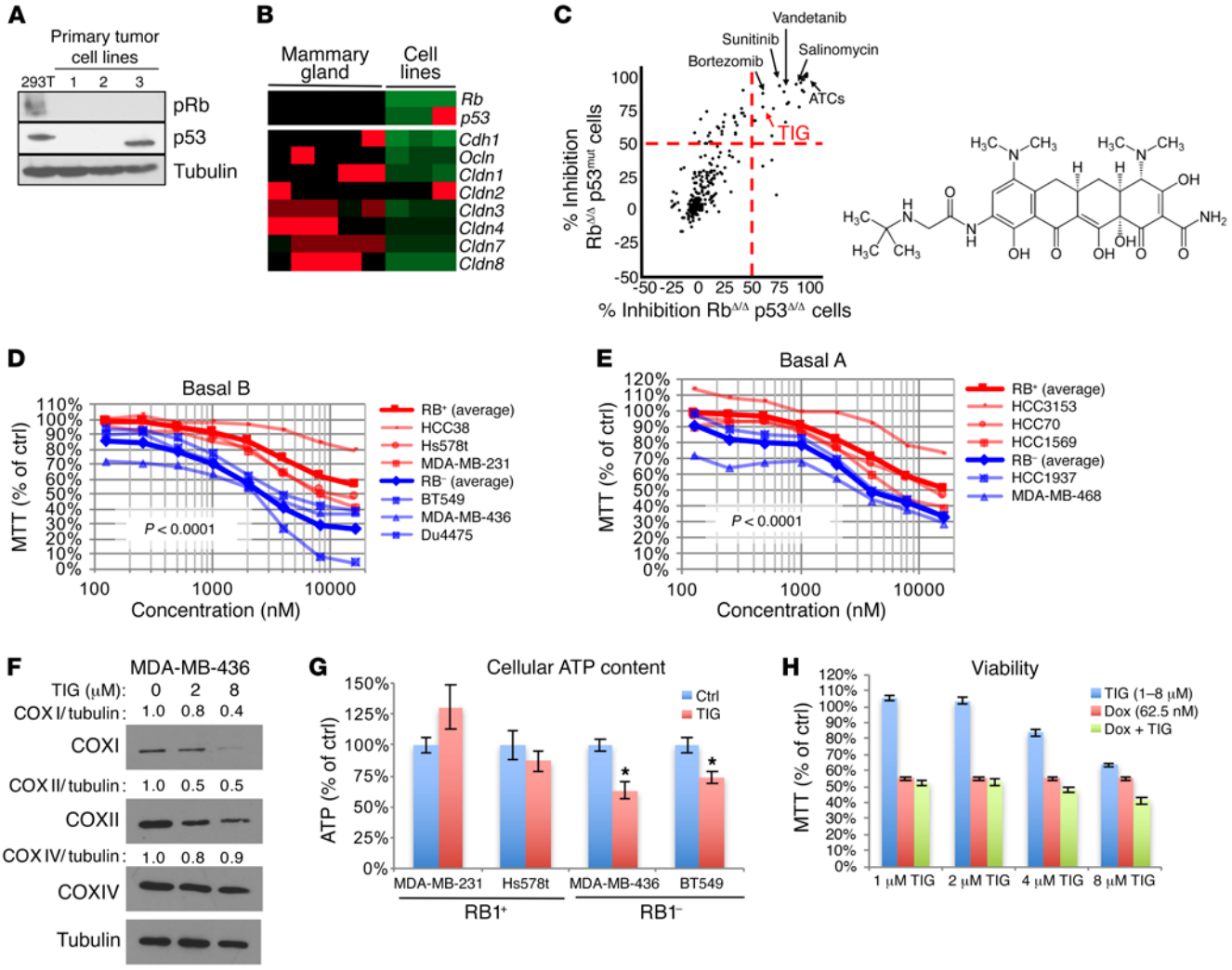

Figure 8. FDA-approved drug screens of Rb/p53-deficient tumors identify TIG, an MPT inhibitor. (**A**) Western blot analysis of pRb and p53 in 3 primary mammary tumor cell lines (lines 1 and 2 $Rb^{\Delta}p53^{\Delta}$; line 3 $Rb^{\Delta}p53^{C139R/+}$). 293T human cells served as a positive control; tubulin was used as a loading control. (**B**) Heatmap showing expression levels of *Rb*, *p53*, and genes associated with the claudin-low subtype in the 3 mouse Rb/p53 lines. (**C**) Scatter plot depicting the inhibitory effects of 312 FDA-approved drugs at a dose of 10 μM in $Rb^{\Delta}p53^{\Delta}$ and $Rb^{\Delta}p53^{mut/+}$ lines and schematic of the molecular structure of TIG. (**D**) TIG dose-response curves for 3 RB1-null and 3 RB1-proficient human claudin-low TNBC cell lines by MTT assay. $P < 0.0001$, by nonlinear regression analysis using GraphPad Prism 6.0. $n = 3$ assays, each performed in sextuplicate. (**E**) TIG dose-response curves for 2 RB1-null and 3 RB1-proficient human basal-like TNBC cell lines. $P < 0.0001$, by nonlinear regression analysis using GraphPad Prism 6.0. $n = 3$, each performed in sextuplicate. (**F**) Western blot for COX I and COX II (mitochondrially translated) and COX IV (cytosolically translated) proteins following TIG treatment. Relative protein levels were normalized to the tubulin loading control. (**G**) Luciferase assay measuring ATP content in TNBC lines after treatment with 2 μM TIG. $n = 3$, performed with 4 to 10 replicates per experiment. $^*P < 0.05$, by 2-tailed *t* test. (**H**) MTT growth assay following combined TIG plus doxorubicin (Dox) on MDA-MB-231 cells. $n = 2$, each performed in triplicate. ctrl, control.

compared it with levels of COX IV and tubulin, which are translated in the cytosol. Three days after transduction, Ad-E2F1 significantly induced COX II n 4 different BC lines ($RB1^+$: MDA-MB-231 and MCF7; $RB1^-$: BT549 and HCC1937) relative to Ad-GFP control, with or without coinfection with Ad-BCL2 (Figure 7B and Supplemental Figure 8).

Finally, we asked whether overexpression of RB1 would suppress MPT genes. We transduced the RB1-deficient BT549 cell line with a recombinant adenovirus encoding WT human RB1, using Ad-GFP as a control. Expression of both MPT genes and known E2F-regulated cell-cycle and apoptotic genes was significantly suppressed by approximately 2-fold 2 days after transduction (Figure 7C). Exceptions were the cell-cycle gene DNA *POLA* and the MPT genes *ATP5D* and *NDUFAB1*, possibly due to low basal mRNA expression of these genes (data not shown). Thus, MPT genes are induced by E2F1 and repressed by pRb as efficiently as are bona fide E2F1–regulated genes.

FDA-approved drug screen identifies TIG, an MPT inhibitor, as a suppressor of Rb/p53-deficient TNBC cell proliferation. In parallel to the above experiments, we performed a repurposing drug screen to identify a potential new therapy for RB1/TP53-mutant TNBC. We isolated 2 primary cell lines (lines 1 and 2) from tumors that developed following transplantation of *MMTV-Cre* $Rb^{fl/fl}$ $p53^{fl/fl}$ MECs and 1 line (line 3) from an *MMTV-Cre* $Rb^{fl/fl}$ tumor that spontaneous-

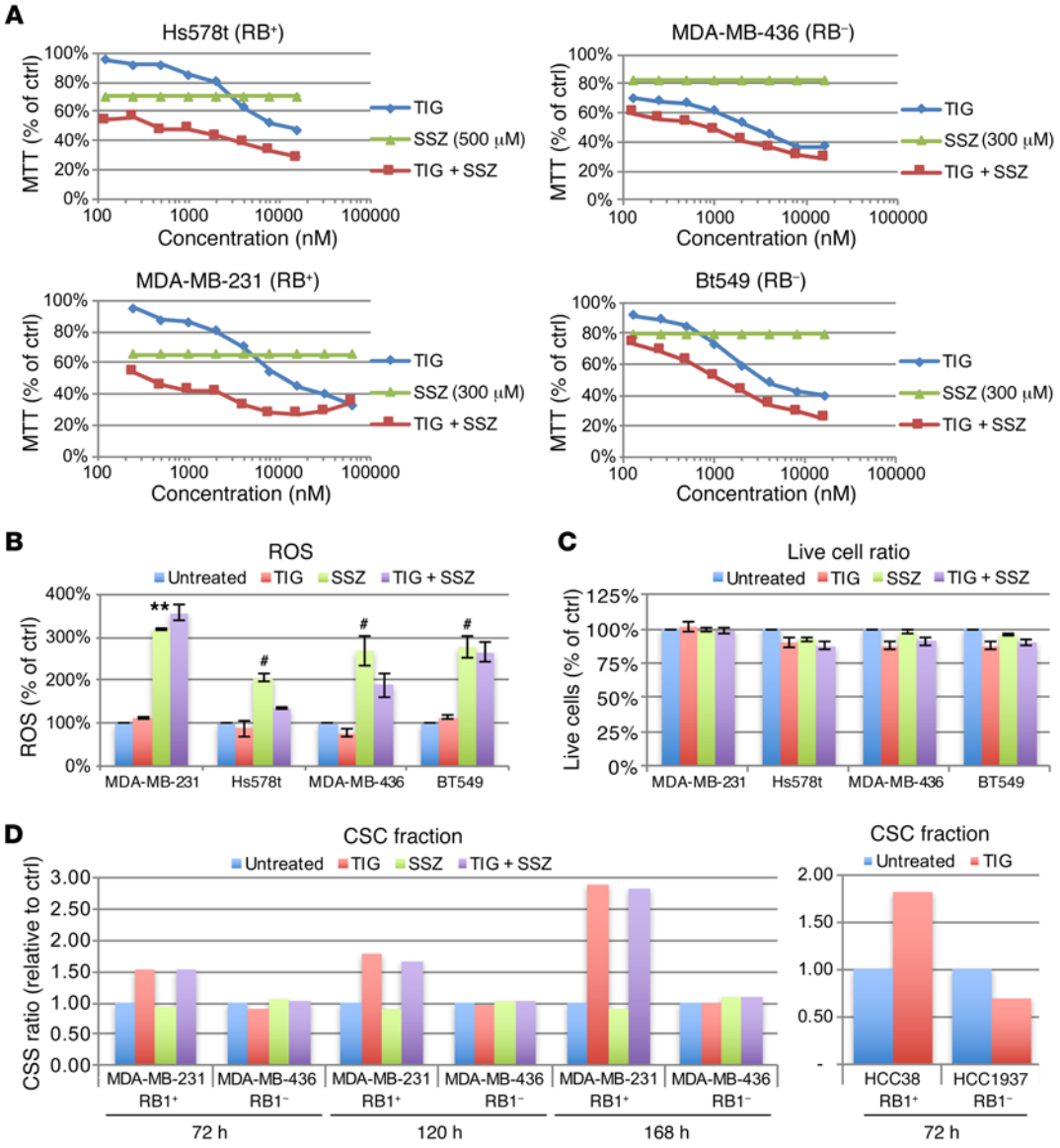

Figure 9. Effects of TIG and SSZ on RB1/TP53-deficient TNBC cell lines. (**A**) MTT assays on RB1-proficient and RB1-deficient TNBC lines treated with the indicated concentrations of TIG; SSZ was used at a dose of 500 μM for Hs578t and 300 μM for MDA-MB-436, MDA-MB-231, and BT549 cells. n = 3–5, each performed in triplicate. (**B**) ROS in TNBC cells 72 hours after treatment with IC_{50} for each line. n = 3; 10,000 events each. $^{**}P < 0.01$ and $^{\#}P$ = ~0.1 , by 2-tailed t test. (**C**) Representative apoptosis assays by annexin V flow cytometry depicting the live-cell fraction 72 hours after treatment with IC_{50} drug concentrations. n = 3; 10,000 events each. (**D**) $CD24^{-}ESA^{+}CD44^{+}$ CSC fractions in TNBC lines 72, 120, and 168 hours after treatment using IC_{50}.

ly acquired a *p53* mutation in the DNA-binding domain (C138R) (5) (Figure 8A). These cells had spindle morphology in tissue culture (Supplemental Figure 9A) and expressed low levels of tight-junction genes including *CDH1, OCLN,* and claudins (Figure 8B).

Using these lines, we screened 312 US Food and Drug Administration–approved (FDA-approved) drugs for a variety of diseases and malignancies (62). A total of 27 compounds at a dose of 10 μM (Figure 8C) and 11 compounds at 1 μM (Supplemental Figure 9B) were found to reduce growth by at least 50% after 3 days of treatment. Top hits from the screens were the anthracyclines (ATCs) (doxorubicin, epirubicin, and idarubicin) currently used to treat TNBC (63). In addition, we identified 2 receptor tyrosine kinase inhibitors (sunitinib and vandetanib), the proteasome inhibitor bortezomib, as well as salinomycin, which had been discovered in a screen for drugs that target BC stem cells (62, 64). These drugs were validated on the 3 $Rb^{\Delta}p53^{\Delta}$ lines (Supplemental Figure 9C).

Strikingly, TIG, an inhibitor of prokaryotic protein translation, was among the most effective drugs in the 10-μM screen (Figure 8C). TIG is a bacteriostatic inhibitor of protein synthesis that binds the 30S ribosomal subunit and blocks entry of aminoacyl–transfer RNA (aminoacyl-tRNA) into the A site of the ribosome during protein translation (65); it was approved by the FDA in 2005 to treat antibiotic-resistant bacteria. Recently, TIG has been found to inhibit acute myeloid leukemia by targeting mammalian MPT (62, 66). As we identified MPT genes as direct targets of pRb-E2F (Figures 4–7), we asked whether TIG could be a viable therapeutic for RB1/TP53-deficient TNBC. We initially used six human claudin-low and basal-B TNBC lines with mutations or deletions

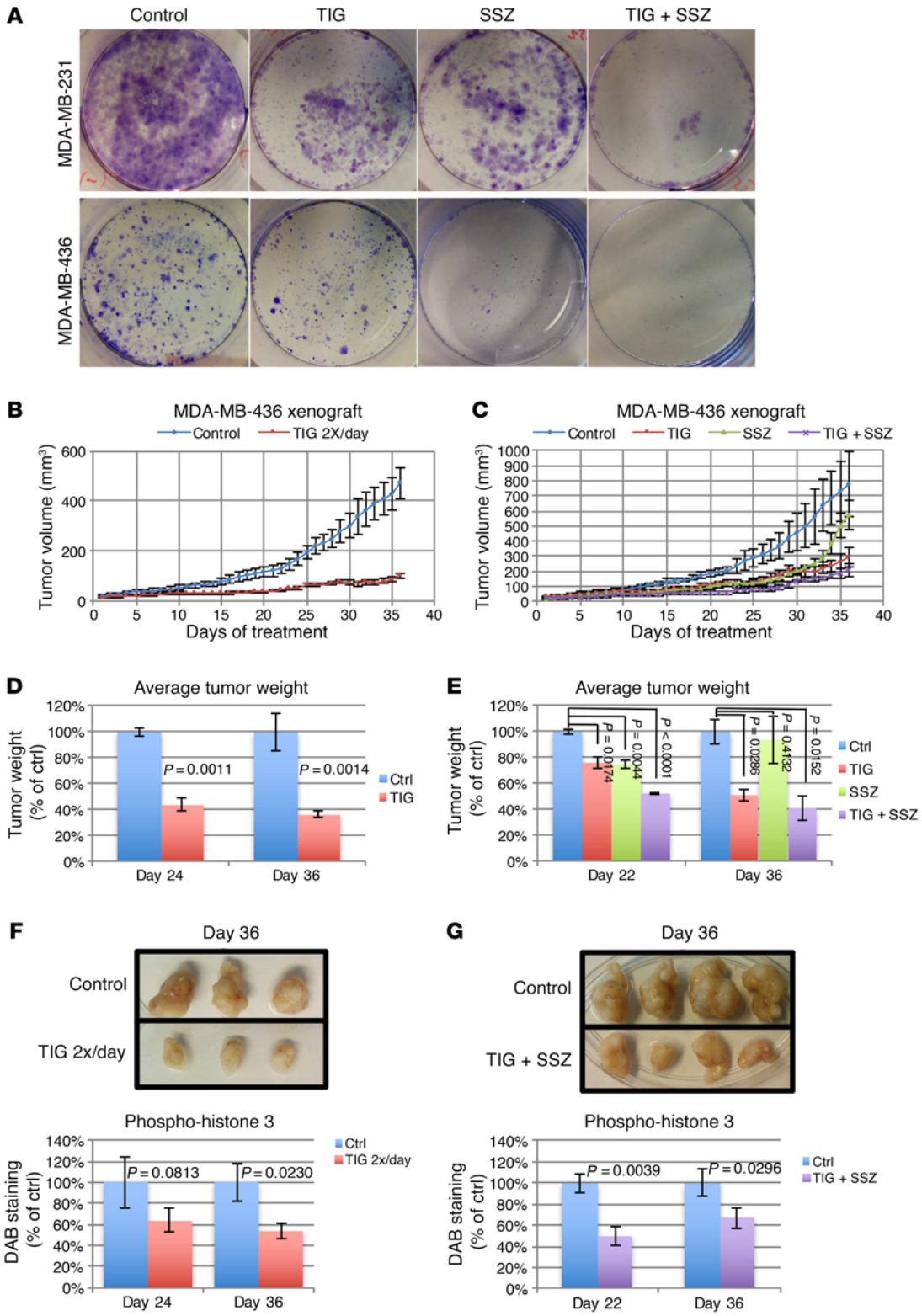

Figure 10. Potent suppression of RB1/TP53-deficient TNBC xenograft growth by TIG with or without SSZ. (**A**) Colony-forming assay for RB1$^+$ MDA-MB-231 and RB1$^-$ MDA-MB-436 cells after 14 days of continuous treatment with IC_{40} for each line. (**B**) Tumor volume of MDA-MB-436 xenografts in NSG mice treated with TIG twice daily (n = 9/group). (**C**) Tumor volume of MDA-MB-436 xenografts treated daily with TIG and/or SSZ (n = 8/group). (**D** and **E**) Average tumor weight following 22 to 24 or 36 days of treatment (endpoint). n = 3–6 per group. (**F** and **G**) Quantification of phospho-histone 3 staining (n = 3). P values were determined by 2-tailed t test.

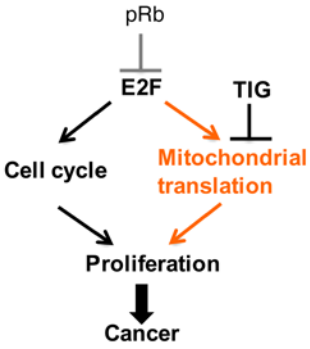

Figure 11. RB1 loss/induction of E2F1 promotes proliferation of TNBC cells by transcriptionally inducing both cell-cycle and MPT genes. Loss of pRb and therefore deregulation of activating E2Fs induce not only cell-cycle genes but also MPT genes, leading to increased MPT. Inhibition of MPT by TIG effectively suppresses cell proliferation and tumor progression in RB1-deficient TNBC.

in *TP53*, three of which also lack functional RB1 (MDA-MB-436, Du4475, and BT49) and three with intact *RB1* (MDA-MB-231, HCC38, and Hs578t) (67, 68). Dose response to TIG revealed that the RB1/TP53-mutant human TNBC cell lines were significantly more sensitive to TIG (average IC_{50}= 3 μM) compared with RB1-proficient/TP53-mutant lines (average IC_{50}>8 μM; $P < 0.0001$; Figure 8D). As these tumor lines are cultured in different media (RPMI or DMEM), we allowed all lines to adapt to RPMI and then retested for TIG sensitivity; under these conditions, the $RB1^-$ lines remained significantly more sensitive to TIG than did the $RB1^+$ lines ($P = 0.0066$).

Next, we tested 5 basal A and basal-like BC lines: 2 $RB1^-$ (HCC1937 and MDA-MB-468) and 3 $RB1^+$ (HCC3153, HCC70, and HCC1569) (67, 68), all cultured in RPMI. Importantly, the RB1-deficient basal A lines also showed a significant increase in TIG sensitivity compared with the $RB1^+$ lines ($P < 0.0001$; Figure 8E). Thus, although the RB1-E2F complex is likely one of several factors that control MPT, RB1 deficiency consistently correlated with an enhanced response to TIG in both claudin-low and basal-like BC cells, at least in these 11 TNBC lines. Notably, in most $RB1^+$ TNBC lines, pRb is partially inactivated through hyperphosphorylation (67), suggesting that the actual effect of pRb-E2F on TIG sensitivity is even higher.

TIG treatment reduced the expression of mitochondrially translated COX I and COX II, but not that of cytosolically translated COX IV (Figure 8F). It also suppressed ATP levels in RB1-deficient tumor cells more effectively than in RB1-proficient cell lines (Figure 8G). In the latter assay, ATP levels were not normalized for cell numbers, so the effects reflect reduced ATP and cell proliferation. Taken together, these results indicate that RB1-deficient TNBC cells display an enhanced dependency on MPT in vitro.

TIG cooperates with the MET inhibitor crizotinib and the antioxidant inhibitor sulfasalazine to suppress growth of TNBC cells in vitro. Effective new therapies, especially those directed at signaling pathways, are likely to involve combination treatments with 2 or more drugs, each targeting different tumor vulnerabilities. We therefore asked whether TIG could be used in combination with other antineoplastic drugs. The ATC doxorubicin showed no or only minor cooperation with TIG (Figure 8H and Supplemental Figure 10A). In experiments in which we treated tumor cells with doxorubicin first and then with TIG, or vice versa, we found that when TIG was administered first, it negated the effect of doxorubicin (Supplemental Figure 10B). We attribute this antagonism to the cytostatic effect of TIG on cell proliferation, the latter of which is needed for efficient inhibition by doxorubicin.

As *MET* is amplified in p53-deficient tumors (51) and in our Rb/p53-mutant tumors (Figure 3, C and D), we asked whether TIG could cooperate with the MET (as well as the ALK and ROS proto-oncogene 1 [ROS1]) inhibitor crizotinib, which effectively kills these tumor cells (Supplemental Figure 5). In contrast to doxorubicin, we observed cooperative inhibition between TIG and crizotinib (Supplemental Figure 10C). However, as MET inhibitors have so far failed in clinical trials, possibly due to poor patient selection (69), we looked for an FDA-approved drug that can target TNBC.

The FDA-approved sulfasalazine (SSZ) attenuates the growth of claudin-low TNBC cells more efficiently than do other BC subtypes (70). SSZ targets the xCT antiporter, which is required for cystine transport and GSH production. A review of the published data revealed that RB1 status had no effect on the response to SSZ. In accordance, we found no statistically significant difference in sensitivity to SSZ in the same 6 claudin-low TNBC lines that differentially responded to TIG treatment (Supplemental Figure 10, D and E). To assess for synergism with TIG, we performed single and combination treatments of claudin-low TNBC cell lines with SSZ (300 μM for MDA-MB-231, MDA-MB-436, and BT549; or 500 μM for the more resistant line Hs578t), adding increasing doses of TIG, and observed a range of cooperative inhibition with these 2 drugs (Figure 9A).

Consistent with previously published work (70), SSZ treatment increased ROS levels in all tested TNBC cells (Figure 9B). In contrast, TIG had no detectable effect on ROS, nor did it increase ROS when administered together with SSZ. Notably, we used IC_{50} drug concentrations for each line so their effect could be compared at similar levels of growth inhibition. In keeping with the cytostatic effects of TIG and SSZ, cell death analysis by 7AAD and annexin V flow cytometry revealed that single and even combined SSZ plus TIG treatment (at IC_{50} each) only modestly compromised cell viability (Figure 9C).

To determine whether these drugs targeted the CSC fraction, we performed flow cytometric analysis with Abs against the cell-surface markers ESA, CD24, and CD44. It was previously demonstrated that sorted $CD24^-ESA^+CD44^+$ cells from several BC lines (including those used herein) are enriched for CSCs and thus capable of initiating new tumors following engraftment into immune-deficient mice (71). Using IC_{50} drug concentrations, the $CD24^-ESA^+CD44^+$ CSC fraction was unaffected 72, 120, and 168 hours after TIG and/or SSZ treatment in the RB1-deficient TNBC line MDA-MB-436. However, exposure to TIG (but not to SSZ) steadily increased the relative percentage of CSCs in the RB1-proficient MDA-MB-231 cell line by 2.88-fold (Figure 9D and Supplemental Figure 11). We extended this analysis to 2 other TNBC lines with discernible $CD24^-ESA^+CD44^+$ CSC populations: basal A/basal-like $RB1^-$ HCC1937 and basal B/claudin-low $RB1^+$ HCC38. Again, TIG treatment increased the CSC fraction in the RB1-proficient line by 1.62-fold but reduced this fraction to 0.69 in

the RB1-deficient line (Figure 9D). Thus, TIG not only abrogates the growth of RB1$^-$ claudin-low TNBC more effectively than do RB1$^+$ cells, it also enriches for CSCs in at least some RB1$^+$ tumors, potentially leading to relapse. Thus, TIG should preferentially be used to treat RB1-deficient TNBC cells.

TIG monotherapy potently inhibits xenograft growth of RB1$^-$/TP53$^-$, but not RB1$^+$/TP53$^-$, TNBC and further cooperates with SSZ in vivo. As a prelude to long-term xenograft assays, we determined the effect of TIG and SSZ either alone or in combination (using IC_{40} for each) on the growth of TNBC lines over a 2-week period, replenishing the drugs twice a week. On both RB1-deficient MDA-MB-436 and RB1-proficient MDA-MB-231 lines, each drug alone reduced the culture by approximately 50%, while combined TIG plus SSZ treatment almost completely abolished cell growth (Figure 10A).

We next tested the effect of these drugs on the growth of MDA-MB-436 xenografts in immune-deficient NOD/SCID/IL-2Rγ (NSG) mice. For TIG monotherapy, we injected tumor-bearing mice (n = 9) with TIG twice a day at 50 mg/kg and gradually increased the drug concentrations to 75 mg/kg. Control mice (n = 9) were injected with vehicle alone. For the TIG plus SSZ combination treatment, we injected mice (n = 8/group) once a day with TIG as above and/or with SSZ at 250 mg/kg. Tumor volume was calculated by caliper measurement (Figure 10, B and C). In addition, at 22 to 23 days after treatment and at 36 days (endpoint), we measured tumor weights for 3 mice or the remaining mice (n = 5–6) in each group. We observed reductions of 56% and 48% in tumor weights for the twice-daily TIG or TIG plus SSZ therapy by days 22–23, and 63% (P = 0.0014) and 59% (P = 0.0152) reductions at the endpoints, respectively (Figure 10, D and E). SSZ treatment cooperated with TIG until day 25 (Figure 10, C and E), after which the tumors became unresponsive to SSZ. In contrast, TIG treatment strongly inhibited tumor growth throughout the course of these experiments.

Albeit smaller in size, no obvious differences between TIG-treated and control tumors were observed upon pathological analysis (Supplemental Figure 12). However, in accordance with the cytostatic effect of TIG in vitro, staining for phospho-histone H3, a mitotic marker, revealed a reproducible and statistically significant reduction in dividing cells in the TIG-treated arm versus that observed in the control vehicle-treated mice (Figure 10, F and G, and Supplemental Figure 12). Finally, we compared the effect of TIG on RB1$^+$ (MDA-MB-231) versus RB1$^-$ (MDA-MB-436) TNBC xenografts in a parallel experiment using similar drug regimens. TIG treatment significantly delayed the growth kinetics of both xenografts (Supplemental Figure 13). However, TIG treatment only had a significant effect on final tumor size in the RB1$^-$ tumors. Taken together, our results demonstrate that *RB1* loss promotes cancer by coordinating cell-cycle progression with increased MPT and that inhibition of the latter suffices to suppress cell proliferation and growth of RB1-deficient TNBC (Figure 11).

Discussion

Inactivation of the RB1 and TP53 tumor suppressors, either individually or in combination, has long been implicated in the genesis of numerous human cancers including BC. Here, we estimated that these 2 tumor suppressors are inactivated together in approximately 28% to 40% of patients with TNBC. In the mouse, we showed that combined mutations in *Rb* and *p53* led to tumors with prominent spindle-cell/mesenchymal–like histology, which clustered closely with human claudin-low TNBC. Although claudin-low/mesenchymal tumors are rare in primary biopsies (46, 72), mesenchyme-like cancer cells are observed in human breast tumors and may represent CSCs that drive relapse and resistance to chemotherapy. Thus, while our Rb/p53-deficient tumors represent an exaggerated form of this phenotype, their analysis may uncover novel mechanisms for targeting these critical BC cells (73).

Through comparison of Rb/p53- versus p53-deficient tumors, bioinformatics, and functional, cell biological, and biochemical analyses, we uncovered a direct role for RB1 in MPT. In addition, in a nonbiased drug screen, we identified TIG, an MPT inhibitor, as a potent growth suppressor of Rb/p53-deficient mouse spindle-cell tumors. TIG preferentially inhibited the proliferation of both TICs and non-TICs in human RB1-deficient/TP53-negative TNBC lines both in vitro and in xenograft assays. Thus, we show that *RB1* loss coordinates cell-cycle progression with increased mitochondrial activity, leading to enhanced sensitivity to TIG, and that inhibition of MPT in TNBC suffices to suppress cell proliferation. Our results complement a previous observation that the repressor p130-E2F4 complex attenuates growth by inhibiting genes involved in both cell-cycle and mitochondrial biogenesis and metabolism (74), some of which overlap with the MPT genes we demonstrate herein to be regulated by activating E2Fs in response to *RB1* loss.

Our observation that *RB1* loss stimulates mitochondrial function rather than anabolic metabolism suggests that enhanced mitochondrial activity and ATP production are critical for cancer progression. While intriguing, this new metabolic role of RB1 is consistent with previous reports suggesting that its inactivation enhances migration in vitro and metastasis in vivo (75, 76). Whereas glycolysis promotes rapid macromolecule synthesis and cell proliferation, recent evidence suggests that cancer cell invasion and dissemination, the prerequisite for metastasis, consume a substantial amount of energy and depend on mitochondrial function and OXPHOS (77, 78). This, however, may be context specific, as the mitochondrial biogenesis factor PGC-1α promotes metastasis in BC but suppresses metastasis in prostate cancer (79). Yet, it is clear that certain oncogenes and tumor suppressors (PI3K, MYC, p53) drive anabolic metabolism, whereas others, like *RB1* loss, as shown herein, promote mitochondrial function and OXPHOS. These opposing metabolic states probably have different impacts on cancer proliferation and dissemination. We propose that the "right" balance between glycolysis and OXPHOS may endow tumor cells with the ability to both proliferate and invade and that this balance may depend on the specific oncogenic networks that are activated in a particular cancer cell.

Cooperation between pRb and p53 is attributed to p53-mediated apoptosis induced by *Rb* loss and other genetic interactions (80, 81). Our results raise the possibility that these 2 tumor suppressors may also cooperate by establishing a metabolic environment conducive to both rapid cell proliferation and invasion and metastasis. Indeed, while *Rb* loss is shown here to promote MPT, p53 deficiency not only promotes glycolysis but also protects mitochondria from permeabilization and cell death, which are induced

by WT TP53 in response to various genotoxic stresses (82). Notably, the inhibitory effect of TIG on cell proliferation suggests that induction of MPT in response to *RB1* loss may be coupled to its effect on cell growth and not only on invasion. Additional experimentation is required to test these hypotheses.

TIG concentrations that inhibited RB1$^+$ TNBC cells (~8 μM) are similar to those found effective for leukemia (62), whereas those that inhibited RB1-deficient cells were significantly lower (~3 μM). In humans, TIG plasma concentrations of 5 μM have been safely achieved (83). Moreover, analysis of patients' plasma following TIG infusions reveals that C_{max} and calculated AUC (0–24 hours) values are considerably higher (AS, unpublished observations). Thus, serum TIG levels far exceed the IC_{50} of RB1-deficient TNBC cells and should be therapeutic. Our results point to a vulnerability of RB1-deficient TNBC that can be exploited therapeutically with TIG or second-generation inhibitors, but other MPT inhibitors may be explored to target these aggressive tumors.

Methods

Identification of RB1/TP53 double-mutant BC patients

The Breast Invasive Carcinoma data set (3) was mined using cBioPortal (84, 85). Patients with combined *RB1* and *TP53* alterations were identified manually using the Download option. *RB* loss Sig$^+$ and p53 activity-low BC patients were identified in Gene Expression Omnibus (GEO) repository data sets (GSEs 2034, 2603, 5327, 6532, 11121, and 25066). The values of gene expression were median centered and visualized as heatmaps. Patients with over 90% of genes above the median were considered *RB* loss Sig$^+$. Significance of overlap of patients was calculated by hypergeometric distribution with "phyper" in R.

Mice

Compound mutant mouse strains were genotyped as previously described (5, 31). *p53$^{LSLR270H/+}$* mice were obtained from the National Cancer Institute (NCI) Mouse Models of Human Cancers Consortium (32). Compound mutant mice were on a mixed background.

Cell lines

TMCRP1, TMCRP2, TMCRP3, RB400, TC53-120, TC53-127, MDA-MB-231, and Hs578T cells were maintained in DMEM containing 10% FBS and 1% penicillin/streptomycin (PEST) at 37°C with 5% CO_2. MDA-MB-436 was maintained in DMEM containing 10% FBS, 1% PEST, and 10 μg/ml insulin. HCC38, Du4475, and BT549 were maintained in RPMI containing 10% FBS and 1% PEST. TMCRP1, TMCRP2, TMCRP3, RB400, TC53-120, and TC53-127 mouse lines were generated in this laboratory. BT549, MDA-MB-436, and MDA-MB-231 cell lines were gifts of the late Mona Gauthier. The remaining lines were purchased from the America Type Culture Collection.

Primary cell isolation, lineage depletion, and 3D culture

MECs were isolated and lineage depleted (47). FACS-sorted luminal and basal cell populations were cultured as previously described (44).

Histology, IHC, and immunoblotting

The following Abs were used: vimentin (1:100; clone D21H3 XP) and E-cadherin (1:400; clone 24E10) from Cell Signaling Technology. Secondary biotinylated anti-rabbit IgG Ab (Vector Laboratories) was used at a dilution of 1:200. For post-treated xenografts, sections were probed with rabbit anti-human cleaved caspase-3 Ab (Cell Signaling Technology; catalog 9661) or rabbit anti-human phospho-histone 3 (catalog CST-9701). The following Abs were used for immunoblotting: RB1 (BD Pharmingen; G3-245), p53 (1:1,000, CST-1C12), rabbit anti-human COX I (1:500; Thermo Fisher Scientific; catalog 26688); rabbit anti-human COX I (1:500; Thermo Fisher Scientific; catalog PA5-26688); rabbit anti-human COX II (1:1,000; Abcam; catalog ab79393); rabbit anti-human COX IV (1:1,000; Cell Signaling Technology; catalog 4844). For COX expression, *n*-dodecyl-B-D-maltoside (Thermo Fisher Scientific; catalog 89902) was used to solubilize membrane proteins.

FACS

The following Abs were used: anti-CD49f conjugated with R-phycoerythrin (1:100; BD; CD49f-PE, clone GoH3); anti-CD24 conjugated with FITC (1:200; BD; CD24-FITC; clone M1/69); and 2 ug/ml propidium iodide (BD). Cell sorting was carried out using a BD FACSAria 11-color cell sorter (Aria GC BRU or Aria II RITT BRV) at 20 psi, and flow cytometry with a BD 4-color FACSCalibur system.

Ad-*Cre* infection

Primary MECs were counted and plated on 24-well low-attachment plates in growth media (without Matrigel) and infected with Ad-CMV-IRES-GFP or Ad-CMV-*Cre*-IRES-GFP (Vector BioLabs) using an MOI of 50 for 1 to 2 hours at 37°C, mixed by gentle pipetting every 15 minutes. After infection, cells were washed 3 times in HBSS supplemented with 2% FBS (HF) and returned to culture for PCR analysis or counted for transplantation. For infection of sorted luminal and basal cells, organoids were collected after 5 to 8 days of culture by gentle centrifugation (130 *g*) for 5 minutes and dissociated in 0.05% trypsin (Sigma-Aldrich) for 5 to10 minutes (basal organoids) or 10 to 20 minutes (luminal organoids), passed through a 40-μm strainer, and infected as above.

Transplantation

Isolated bulk, sorted primary mammary, or tumor cells were resuspended in 10 μl HF mixed 1:1 with 10 μl Matrigel and injected into the fourth inguinal mammary glands of 3- to 4-week-old immune-deficient mice. Ad-CMV-*Cre*-IRES-GFP–infected cells (1×10^4 to 3×10^4) were transplanted into cleared mammary fat pads.

Gene expression

Affymetrix Mouse Gene 1.0 ST arrays were analyzed as described previously (56, 86). Differentially expressed genes were identified by ANOVA (FDR = 0.05). Data were integrated by distance-weighted discrimination (DWD) (87, 88), using shared intrinsic genes and unsupervised hierarchical clustering (average linkage).

DNA copy number

Mouse SurePrint G3 1M arrays were analyzed at The Centre for Applied Genomics (operated by the Hospital for Sick Children) using tail DNA pooled from 5 *Rb$^{fl/fl}$ p53$^{fl/fl}$* mice as a reference and Nexus Copy Number software, version 6.0 (BioDiscovery). Normalized and median-centered $\log_2$ ratios of genes of interest were visualized by heatmaps (Partek).

Pathway enrichment

Gene expression data were analyzed using GSEA (54), with parameters set to 2,000 gene set permutations and a gene sets size between 8 and 500, and were analyzed as described previously (55), with a nominal *P* value of less than 0.005, an FDR *q* value of less than 0.05, and an overlap coefficient of 0.5.

E2F transcription binding site (oPOSSUM 3.0) and recruitment (ENCODE and ChIP-on-chip)

2,000-bp upstream and 1,000-bp downstream sequences from the TSS of upregulated genes (FDE ≤0.05) were analyzed using oPOSSUM 3.0 (default parameters) (http://opossum.cisreg.ca/oPOSSUM3/) (57). Genes harboring an E2F1 motif (JASPAR database ID: MA0024.1) within the –2 kb to +1 kb window were retrieved for the "mitochondrial translation" pathway module. Human orthologs for the MPT genes with consensus E2F binding sites were retrieved using BioMart-Ensembl (*Homo sapiens* GRCh39 and *Mus musculus* GRCm38.p2). Peaks from ENCODE ChIP-seq data for the BC cell line MCF7 targeted by the HA-E2F1 Ab (GEO GSM935477, narrowPeak) located within –2 kb to +1 kb of these orthologous genes were retrieved using the Genomic Regions Enrichment of Annotations Tool (GREAT) (89), and corresponding tracks were visualized using the UCSC genome browser (GRCh37/hg19).

For ChIP-chip analysis, the Hg17-built ChIP-on-chip data sets (NimbleGen_1500b_Promoter_Array, GPL4599) of E2F1 binding in MCF7 and MCF10A cells were downloaded from the NCBI's GEO data sets (GSE 8716). Genomic locations of the GPL4599-hg17 binding sites were converted to hg19 by UCSC LiftOver (http://genome.ucsc.edu/cgi-bin/hgLiftOver) for comparison with ENCODE. Initial analysis was performed using BioConductor package ACME in R, with the window size at 1,000 bp to obtain *P* values for each genomic probe. Two thousand permutations were carried out using ACME-generated *P* values to calculate empirical *P* values (ePV) using ACME parameters set to 1,000 bp as the window size, 0.85 as the threshold, and 0.05 as ePV cutoff.

Correlation analysis

Expression levels of RB1 and E2F1-3 genes in different BC subtypes were determined in six GPL96 cohorts (GEO GSEs 2034, 2603, 5327, 6532, 11121, and 25066). Each data set was analyzed independently by obtaining the robust multiarray average–normalized (RMA-normalized) expression value of individual cohorts and normalizing by median expression. Data from each cohort was $\log_2$ transformed and median centered, followed by Pearson's linear correlation *r* and *P* value calculations using the paleontological statistics software package for education and data analysis PAST as previously described (29).

qRT-PCR

qRT-PCR was performed using Power SYBR Master Mix on a 7900HT Fast Real-Time PCR System (both from Applied Biosystems) and the comparative threshold cycle method (ΔΔCt). All reactions were performed in triplicate in at least 3 separate experiments. Relative gene expression was normalized to *GAPDH* and calibrated to the control. The primers used are listed in Supplemental Figure 14.

Retroviral and adenoviral E2F and RB1 transduction

Phoenix Ampho cells were transfected with pBABE encoding MYC-tagged E2F3a or E2F3b cDNAs, and viral media were collected 48 hours later. MDA-MB-231 cells (1×10^6) were plated and incubated with viral media at 37°C for 48 hours. E2F3-expressing and puromycin-resistant clones were selected for 2 weeks in 300 μg/ml puromycin-containing media.

High-titer recombinant adenovirus particles Ad-E2F1 (ADV-207490), Ad-BCL2 (catalog 1412), Ad-GFP (catalog 1060), and Ad-RB1 (catalog 1043) were purchased from Vector BioLabs. Cells were seeded so that after 2 or 3 days they would be up to 80% confluent and infected with an MOI of 500.

Drug screen, validation, and MTT viability assays

The Sequoia Library (Pangbourne, United Kingdom) was screened as previously described (33, 90). Chemicals were purchased from Sigma-Aldrich (doxorubicin, epirubicin, idarubicin, SSZ); Selleck Chemicals (sunitinib, salinomycin, TIG, crizotinib); Tocris (WAY 170523); and Sequoia Research Products (TIG). MTT assays were performed as described previously (90).

ATP quantification and ROS analysis

Cellular ATP levels were determined using the CellTiter-Glo Luminescent Cell Viability Assay (Promega). For ROS, 2′,7′-dichlorofluorescin diacetate (DCF; Sigma-Aldrich) was added to cell media to a final concentration of 20 μM and incubated at 37°C for 3 hours. Cells were analyzed on a BD FACSCaliber system within 1 hour after staining.

CSCs and apoptosis

Cells were incubated with mouse anti-human ESA/Ep-CAM/CD326-PE (BioLegend), CD24-FITC (BD), and CD44-APC (BD) Abs on ice, followed by 7-AAD, and processed on a BD FACSCaliber system within 1 hour after staining. A BD Annexin V–PE Kit was used for the apoptosis assay.

Long-term in vitro and xenograft analysis

Drugs were replaced twice weekly for 2 weeks, and cells were fixed in 10% formalin for 5 minutes and stained with 0.05% Crystal Violet (Sigma-Aldrich). For SSZ and TIG xenograft assays, NSG mice were injected with 1×10^6 MDA-MB-436 cells into inguinal fat pads. Once palpable tumors formed (~14 mm^3, 3 weeks after injection), mice were randomized and treated 6 days per week for 5 weeks.

Combination experiments. Mice were treated i.p. once per day with 50 mg/kg TIG, 250 mg/kg SSZ, a combination of both, or with vehicle alone. Drugs were prepared fresh each day.

Double-dose TIG experiments. Mice were treated i.p. twice per day with saline or 50 mg/kg TIG for the first week, 62.5 mg/kg TIG the second week, and 75 mg/kg TIG for the remaining time.

$RB1^+$ versus $RB1^-$ comparison. Cells (1×10^6) (MDA-MB-436 or MDA-MB-231) were injected, and, once palpable tumors were detected, mice were treated twice per day with 50 mg/kg TIG. Tumor volumes were measured by caliper 5 times per week.

Statistics

Comparison of 2 means was performed using a 2-tailed Student's *t* test. Multiple sample comparisons were calculated using ANOVA, followed by Tukey's post-hoc analysis. Kaplan-Meier plots were generated using GraphPad Prism, version 6.0 (GraphPad Software), and *P* values for curve comparisons were calculated using the Mantel-Cox

(log-rank) method. Differences between values were considered statistically significant at a *P* value of less than 0.05. TIC frequency was estimated by Poisson distribution using L-Calc Software, version 1.1.1 (STEMCELL Technologies). All data represent SD.

Study approval

Animal protocols were approved by the University Health Network (Toronto, Ontario, Canada) in accordance with Canadian Council of Animal Care guidelines.

Author contributions

RAJ, TJR, JCL, MS, VV, GDB, ZJ, AS, and EZ designed the research studies. RAJ, TJR, JCL, MS, YJ, PEDC, VLF, ZJ, and EZ conducted experiments and analyzed data. RAJ, JCL, VV, GP, LM, SB, GL, and GDB carried out bioinformatics analyses. GDB, AD, and AS oversaw bioinformatic analysis, robotic high-throughput screens, and TIG experiments, respectively. RAJ, TJR, JCL, MS, VV, ZJ, SEE, AS, and EZ wrote the manuscript. All authors made comments on the manuscript.

Acknowledgments

This study was conducted with support from a US Army Department of Defense Breast Cancer Research Program Postdoctoral Fellowship Award (W81XWH-10-1-0689, to RAJ); the NIH (GM103504, to GDB); the Canadian BC Foundation (Ontario Chapter); the Canadian Cancer Society (020456, to EZ); and the Terry-Fox Foundation (to SEE and EZ).

Address correspondence to: Eldad Zacksenhaus, Toronto General Research Institute - University Health Network, 67 College Street, Room 407, Toronto, Ontario, Canada M5G 2M1. Phone: 416.340.4800 ext. 5106; E-mail: eldad.zacksenhaus@utoronto.ca.

1. Prat A, Perou CM. Deconstructing the molecular portraits of breast cancer. *Mol Oncol*. 2011;5(1):5–23.
2. Curtis C, et al. The genomic and transcriptomic architecture of 2,000 breast tumours reveals novel subgroups. *Nature*. 2012;486(7403):346–352.
3. Cancer Genome Atlas Network. Comprehensive molecular portraits of human breast tumours. *Nature*. 2012;490(7418):61–70.
4. Nik-Zainal S, et al. Landscape of somatic mutations in 560 breast cancer whole-genome sequences. *Nature*. 2016;534(7605):47–54.
5. Jiang Z, et al. Rb deletion in mouse mammary progenitors induces luminal-B or basal-like/EMT tumor subtypes depending on p53 status. *J Clin Invest*. 2010;120(9):3296–3309.
6. Morris EJ, Dyson NJ. Retinoblastoma protein partners. *Adv Cancer Res*. 2001;82:1–54.
7. St-Pierre B, et al. Conserved and specific functions of mammalian ssu72. *Nucleic Acids Res*. 2005;33(2):464–477.
8. Zacksenhaus E, Jiang Z, Phillips RA, Gallie BL. Dual mechanisms of repression of E2F1 activity by the retinoblastoma gene product. *EMBO J*. 1996;15(21):5917–5927.
9. Liu H, et al. Redeployment of Myc and E2f1-3 drives Rb-deficient cell cycles. *Nat Cell Biol*. 2015;17(8):1036–1048.
10. Chen HZ, Tsai SY, Leone G. Emerging roles of E2Fs in cancer: an exit from cell cycle control. *Nat Rev Cancer*. 2009;9(11):785–797.
11. Ciavarra G, Zacksenhaus E. Direct and indirect effects of the pRb tumor suppressor on autophagy. *Autophagy*. 2011;7(5):544–546.
12. Burkhart DL, Sage J. Cellular mechanisms of tumour suppression by the retinoblastoma gene. *Nat Rev Cancer*. 2008;8(9):671–682.
13. Knudsen ES, Knudsen KE. Tailoring to RB: tumour suppressor status and therapeutic response. *Nat Rev Cancer*. 2008;8(9):714–724.
14. Rabinovich A, Jin VX, Rabinovich R, Xu X, Farnham PJ. E2F in vivo binding specificity: comparison of consensus versus nonconsensus binding sites. *Genome Res*. 2008;18(11):1763–1777.
15. Turner NC, Reis-Filho JS. Tackling the diversity of triple-negative breast cancer. *Clin Cancer Res*. 2013;19(23):6380–6388.
16. Jiang Z, et al. RB1 and p53 at the crossroad of EMT and triple-negative breast cancer. *Cell Cycle*. 2011;10(10):1563–1570.
17. Vander Heiden MG, Cantley LC, Thompson CB. Understanding the Warburg effect: the metabolic requirements of cell proliferation. *Science*. 2009;324(5930):1029–1033.
18. Koppenol WH, Bounds PL, Dang CV. Otto Warburg's contributions to current concepts of cancer metabolism. *Nat Rev Cancer*. 2011;11(5):325–337.
19. Cairns RA, Harris IS, Mak TW. Regulation of cancer cell metabolism. *Nat Rev Cancer*. 2011;11(2):85–95.
20. Pavlova NN, Thompson CB. The emerging hallmarks of cancer metabolism. *Cell Metab*. 2016;23(1):27–47.
21. Nicolay BN, et al. Loss of RBF1 changes glutamine catabolism. *Genes Dev*. 2013;27(2):182–196.
22. Reynolds MR, et al. Control of glutamine metabolism by the tumor suppressor Rb. *Oncogene*. 2014;33(5):556–566.
23. Ciavarra G, Zacksenhaus E. Rescue of myogenic defects in Rb-deficient cells by inhibition of autophagy or by hypoxia-induced glycolytic shift. *J Cell Biol*. 2010;191(2):291–301.
24. Váraljai R, Islam AB, Beshiri ML, Rehman J, Lopez-Bigas N, Benevolenskaya EV. Increased mitochondrial function downstream from KDM5A histone demethylase rescues differentiation in pRB-deficient cells. *Genes Dev*. 2015;29(17):1817–1834.
25. Takahashi C, Sasaki N, Kitajima S. Twists in views on RB functions in cellular signaling, metabolism and stem cells. *Cancer Sci*. 2012;103(7):1182–1188.
26. Lopez-Mejia IC, Fajas L. Cell cycle regulation of mitochondrial function. *Curr Opin Cell Biol*. 2015;33:19–25.
27. Nicolay BN, et al. Proteomic analysis of pRb loss highlights a signature of decreased mitochondrial oxidative phosphorylation. *Genes Dev*. 2015;29(17):1875–1889.
28. Gatza ML, et al. A pathway-based classification of human breast cancer. *Proc Natl Acad Sci U S A*. 2010;107(15):6994–6999.
29. Liu JC, et al. Combined deletion of Pten and p53 in mammary epithelium accelerates triple-negative breast cancer with dependency on eEF2K. *EMBO Mol Med*. 2014;6(12):1542–1560.
30. Herschkowitz JI, He X, Fan C, Perou CM. The functional loss of the retinoblastoma tumour suppressor is a common event in basal-like and luminal B breast carcinomas. *Breast Cancer Res*. 2008;10(5):R75.
31. Wagner KU, Boulanger CA, Henry MD, Sgagias M, Hennighausen L, Smith GH. An adjunct mammary epithelial cell population in parous females: its role in functional adaptation and tissue renewal. *Development*. 2002;129(6):1377–1386.
32. Olive KP, et al. Mutant p53 gain of function in two mouse models of Li-Fraumeni syndrome. *Cell*. 2004;119(6):847–860.
33. Wang S, Liu JC, Kim D, Datti A, Zacksenhaus E. Targeted Pten deletion plus p53-R270H mutation in mouse mammary epithelium induces aggressive claudin-low and basal-like breast cancer. *Breast Cancer Res*. 2016;18(1):9.
34. Damonte P, Gregg JP, Borowsky AD, Keister BA, Cardiff RD. EMT tumorigenesis in the mouse mammary gland. *Lab Invest*. 2007;87(12):1218–1226.
35. Herschkowitz JI, et al. Identification of conserved gene expression features between murine mammary carcinoma models and human breast tumors. *Genome Biol*. 2007;8(5):R76.
36. Pattabiraman DR, Weinberg RA. Tackling the cancer stem cells - what challenges do they pose? *Nat Rev Drug Discov*. 2014;13(7):497–512.
37. Creighton CJ, et al. Residual breast cancers after conventional therapy display mesenchymal as well as tumor-initiating features. *Proc Natl Acad Sci U S A*. 2009;106(33):13820–13825.
38. Visvader JE. Cells of origin in cancer. *Nature*. 2011;469(7330):314–322.
39. Lim E, et al. Aberrant luminal progenitors as the candidate target population for basal tumor development in BRCA1 mutation carriers. *Nat Med*. 2009;15(8):907–913.
40. Oakes SR, Gallego-Ortega D, Ormandy CJ. The mammary cellular hierarchy and breast cancer. *Cell Mol Life Sci*. 2014;71(22):4301–4324.
41. Prat A, Perou CM. Mammary development meets cancer genomics. *Nat Med*. 2009;15(8):842–844.
42. Stingl J, et al. Purification and unique properties of mammary epithelial stem cells. *Nature*.

2006;439(7079):993–997.
43. Shackleton M, et al. Generation of a functional mammary gland from a single stem cell. *Nature*. 2006;439(7072):84–88.
44. Guo W, et al. Slug and Sox9 cooperatively determine the mammary stem cell state. *Cell*. 2012;148(5):1015–1028.
45. Rijnkels M, Rosen JM. Adenovirus-Cre-mediated recombination in mammary epithelial early progenitor cells. *J Cell Sci*. 2001;114(Pt 17):3147–3153.
46. Prat A, et al. Phenotypic and molecular characterization of the claudin-low intrinsic subtype of breast cancer. *Breast Cancer Res*. 2010;12(5):R68.
47. Liu JC, Deng T, Lehal RS, Kim J, Zacksenhaus E. Identification of tumorsphere- and tumor-initiating cells in HER2/Neu-induced mammary tumors. *Cancer Res*. 2007;67(18):8671–8681.
48. Ohta M, et al. The FHIT gene, spanning the chromosome 3p14.2 fragile site and renal carcinoma-associated t(3;8) breakpoint, is abnormal in digestive tract cancers. *Cell*. 1996;84(4):587–597.
49. Negrini M, et al. The FHIT gene at 3p14.2 is abnormal in breast carcinomas. *Cancer Res*. 1996;56(14):3173–3179.
50. Cheng L, et al. Rb inactivation accelerates neoplastic growth and substitutes for recurrent amplification of cIAP1, cIAP2 and Yap1 in sporadic mammary carcinoma associated with p53 deficiency. *Oncogene*. 2010;29(42):5700–5711.
51. Knight JF, et al. Met synergizes with p53 loss to induce mammary tumors that possess features of claudin-low breast cancer. *Proc Natl Acad Sci U S A*. 2013;110(14):E1301–E1310.
52. Zou HY, et al. An orally available small-molecule inhibitor of c-Met, PF-2341066, exhibits cytoreductive antitumor efficacy through antiproliferative and antiangiogenic mechanisms. *Cancer Res*. 2007;67(9):4408–4417.
53. Chen JM, et al. Structure-based design of a novel, potent, and selective inhibitor for MMP-13 utilizing NMR spectroscopy and computer-aided molecular design. *J Am Chem Soc*. 2000;122(40):9648–9654.
54. Subramanian A, et al. Gene set enrichment analysis: a knowledge-based approach for interpreting genome-wide expression profiles. *Proc Natl Acad Sci U S A*. 2005;102(43):15545–15550.
55. Merico D, Isserlin R, Stueker O, Emili A, Bader GD. Enrichment map: a network-based method for gene-set enrichment visualization and interpretation. *PLoS One*. 2010;5(11):e13984.
56. Liu JC, et al. Seventeen-gene signature from enriched Her2/Neu mammary tumor-initiating cells predicts clinical outcome for human HER2+:ERα- breast cancer. *Proc Natl Acad Sci U S A*. 2012;109(15):5832–5837.
57. Kwon AT, Arenillas DJ, Worsley Hunt R, Wasserman WW. oPOSSUM-3: advanced analysis of regulatory motif over-representation across genes or ChIP-Seq datasets. *G3 (Bethesda)*. 2012;2(9):987–1002.
58. Kellis M, et al. Defining functional DNA elements in the human genome. *Proc Natl Acad Sci U S A*. 2014;111(17):6131–6138.
59. Wells J, Boyd KE, Fry CJ, Bartley SM, Farnham PJ. Target gene specificity of E2F and pocket protein family members in living cells. *Mol Cell Biol*. 2000;20(16):5797–5807.
60. Levshenkova EV, Ukraintsev KE, Zhugdernamzhilyn O, Kovriga IE, Alibaeva RA, Frolova EI. [Functional studying of promoter region of the human mrpl37 gene]. *Mol Biol (Mosk)*. 2005;39(1):159–162.
61. Ambrus AM, et al. Loss of dE2F compromises mitochondrial function. *Dev Cell*. 2013;27(4):438–451.
62. Skrtić M, et al. Inhibition of mitochondrial translation as a therapeutic strategy for human acute myeloid leukemia. *Cancer Cell*. 2011;20(5):674–688.
63. Gehl J, Boesgaard M, Paaske T, Vittrup Jensen B, Dombernowsky P. Combined doxorubicin and paclitaxel in advanced breast cancer: effective and cardiotoxic. *Ann Oncol*. 1996;7(7):687–693.
64. Gupta PB, et al. Identification of selective inhibitors of cancer stem cells by high-throughput screening. *Cell*. 2009;138(4):645–659.
65. Slover CM, Rodvold KA, Danziger LH. Tigecycline: a novel broad-spectrum antimicrobial. *Ann Pharmacother*. 2007;41(6):965–972.
66. Jhas B, et al. Metabolic adaptation to chronic inhibition of mitochondrial protein synthesis in acute myeloid leukemia cells. *PLoS One*. 2013;8(3):e58367.
67. Robinson TJ, et al. RB1 status in triple negative breast cancer cells dictates response to radiation treatment and selective therapeutic drugs. *PLoS One*. 2013;8(11):e78641.
68. Neve RM, et al. A collection of breast cancer cell lines for the study of functionally distinct cancer subtypes. *Cancer Cell*. 2006;10(6):515–527.
69. Garber K. MET inhibitors start on road to recovery. *Nat Rev Drug Discov*. 2014;13(8):563–565.
70. Timmerman LA, et al. Glutamine sensitivity analysis identifies the xCT antiporter as a common triple-negative breast tumor therapeutic target. *Cancer Cell*. 2013;24(4):450–465.
71. Fillmore CM, Kuperwasser C. Human breast cancer cell lines contain stem-like cells that self-renew, give rise to phenotypically diverse progeny and survive chemotherapy. *Breast Cancer Res*. 2008;10(2):R25.
72. Sabatier R, et al. Claudin-low breast cancers: clinical, pathological, molecular and prognostic characterization. *Mol Cancer*. 2014;13:228.
73. Pattabiraman DR, et al. Activation of PKA leads to mesenchymal-to-epithelial transition and loss of tumor-initiating ability. *Science*. 2016;351(6277):aad3680.
74. Cam H, et al. A common set of gene regulatory networks links metabolism and growth inhibition. *Mol Cell*. 2004;16(3):399–411.
75. Kim KJ, et al. Rb suppresses collective invasion, circulation and metastasis of breast cancer cells in CD44-dependent manner. *PLoS One*. 2013;8(12):e80590.
76. Knudsen ES, McClendon AK, Franco J, Ertel A, Fortina P, Witkiewicz AK. RB loss contributes to aggressive tumor phenotypes in MYC-driven triple negative breast cancer. *Cell Cycle*. 2015;14(1):109–122.
77. Tan AS, et al. Mitochondrial genome acquisition restores respiratory function and tumorigenic potential of cancer cells without mitochondrial DNA. *Cell Metab*. 2015;21(1):81–94.
78. LeBleu VS, et al. PGC-1α mediates mitochondrial biogenesis and oxidative phosphorylation in cancer cells to promote metastasis. *Nat Cell Biol*. 2014;16(10):992–1003.
79. Torrano V, et al. The metabolic co-regulator PGC1α suppresses prostate cancer metastasis. *Nat Cell Biol*. 2016;18(6):645–656.
80. Williams BO, Remington L, Albert DM, Mukai S, Bronson RT, Jacks T. Cooperative tumorigenic effects of germline mutations in Rb and p53. *Nat Genet*. 1994;7(4):480–484.
81. Brosh R, et al. p53-Repressed miRNAs are involved with E2F in a feed-forward loop promoting proliferation. *Mol Syst Biol*. 2008;4:229.
82. Vaseva AV, Marchenko ND, Ji K, Tsirka SE, Holzmann S, Moll UM. p53 opens the mitochondrial permeability transition pore to trigger necrosis. *Cell*. 2012;149(7):1536–1548.
83. Muralidharan G, Micalizzi M, Speth J, Raible D, Troy S. Pharmacokinetics of tigecycline after single and multiple doses in healthy subjects. *Antimicrob Agents Chemother*. 2005;49(1):220–229.
84. Cerami E, et al. The cBio cancer genomics portal: an open platform for exploring multidimensional cancer genomics data. *Cancer Discov*. 2012;2(5):401–404.
85. Gao J, et al. Integrative analysis of complex cancer genomics and clinical profiles using the cBioPortal. *Sci Signal*. 2013;6(269):pl1.
86. Liu JC, et al. Combined deletion of Pten and p53 in mammary epithelium accelerates triple-negative breast cancer with dependency on eEF2K. *EMBO Mol Med*. 2014;6(12):1542–1560.
87. Benito M, et al. Adjustment of systematic microarray data biases. *Bioinformatics*. 2004;20(1):105–114.
88. Liu JC, Wang DY, Egan SE, Zacksenhaus E. Common and distinct features of mammary tumors driven by Pten-deletion or activating Pik3ca mutation. *Oncotarget*. 2016;7(8):9060–9068.
89. McLean CY, et al. GREAT improves functional interpretation of cis-regulatory regions. *Nat Biotechnol*. 2010;28(5):495–501.
90. Robinson TJ, et al. High-throughput screen identifies disulfiram as a potential therapeutic for triple-negative breast cancer cells: interaction with IQ motif-containing factors. *Cell Cycle*. 2013;12(18):3013–3024.